

RESEARCH ARTICLE

10.1029/2018JB015643

Key Points:

- We have conducted 3-D lithospheric-scale numerical modeling of rift interaction
- Extensional reactivation of lithospheric-scale suture zones has been analyzed
- Strike-slip transfer faults evolve and change their sense of shear with time

Supporting Information:

- Supporting Information S1

Correspondence to:

A. Balázs,
balatt@gmail.com

Citation:

Balázs, A., Matenco, L., Vogt, K., Cloetingh, S., & Gerya, T. (2018). Extensional polarity change in continental rifts: Inferences from 3-D numerical modeling and observations. *Journal of Geophysical Research: Solid Earth*, 123, 8073–8094. <https://doi.org/10.1029/2018JB015643>

Received 9 FEB 2018

Accepted 7 AUG 2018

Accepted article online 17 AUG 2018

Published online 4 SEP 2018

Extensional Polarity Change in Continental Rifts: Inferences From 3-D Numerical Modeling and Observations

A. Balázs^{1,2} , L. Matenco¹ , K. Vogt³, S. Cloetingh¹, and T. Gerya⁴

¹Tectonics Group, Department of Earth Sciences, Faculty of Geosciences, Utrecht University, Utrecht, Netherlands, ²Now at Laboratory of Experimental Tectonics, Department of Sciences, Università degli Studi Roma Tre, Rome, Italy, ³International Geothermal Centre, Bochum University of Applied Sciences, Bochum, Germany, ⁴Geophysical Fluid Dynamics Group, Institute of Geophysics, ETH, Zurich, Switzerland

Abstract Extensional basins often show along-strike variability in terms of fault geometries, basement structures, subsidence, and thermal evolution. This is particularly pronounced when extension reactivates preexisting suture zones with opposing dip directions, that is, opposite polarities, which creates wide strike-slip transfer zones. We have studied this extensional variability by means of thermomechanical lithospheric-scale 3-D numerical modeling. We conducted a series of experiments to model the extension of a thick lithosphere simulating a young orogenic area containing segmented suture zones inherited from former opposing subduction polarities, implemented as rheologically weak inclined layers with opposite dips. Numerical experiments demonstrate that the initial subduction sutures are reactivated by two long-lived lithospheric-scale detachment faults, which remain active until the onset of oceanic spreading. The opposite polarity of these faults causes their migration toward each other by asymmetric mantle lithosphere extension and thermal accretion. Crustal kinematics shows the formation of extensional detachment faults and high-offset listric normal faults. These structures undergo gradual tilting during their footwall exhumation, while the rheological weak suture layers are redistributed beneath the crust. The results demonstrate an active interaction along the strike of the system between the two opposite dipping weak zones, where fault segments mechanically interact. During extension, the maximum horizontal fault offset switches the apparent sense of shear in the separating strike-slip transfer zone. This kinematics explain the rapid change in the sense of shear in major strike-slip transfer zones or transform faults, such as observed during the extension of the Pannonian back-arc basin.

1. Introduction

The formation of extensional sedimentary basins is controlled by external and internal forcing factors and parameters, such as variable plate velocities, magmatic and surface processes, and the initial lithospheric thermal and rheological configurations (e.g., Brun, 1999; Burov & Poliakov, 2001; Cloetingh et al., 2013; Dias et al., 2015; Naliboff et al., 2017; Rosenbaum et al., 2005). Extension generally affects a continental lithosphere that contains heterogeneities created by inherited orogenic growth by plate convergence. These heterogeneities localize rifting along rheological contrasts or weak zones, such as former suture zones or major nappe contacts (Bellahsen et al., 2006; Buiter & Torsvik, 2014; Corti, 2009; Dunbar & Sawyer, 1988; Duretz et al., 2016; Heron et al., 2016; Huet et al., 2011; Keranen & Klemperer, 2008). Extensional reactivation of such inherited inclined weak zones creates asymmetric basin systems, where deformation and associated subsidence are controlled by large-scale detachments or low-angle normal faults with high offsets that are inclined predominantly in one direction (Wernicke, 1985). When the continental rift system evolves into passive continental margins, extensional upper and lower plates can be also defined for the original onset of extension along lithospheric-scale detachments (Lister et al., 1986). Such a scenario is inferred at the onset of continental extension in the Atlantic Ocean or in back-arc basins, such as the Aegean or the Pannonian systems (Balázs et al., 2017; Jolivet et al., 2013; Petersen & Schiffer, 2016). When extension takes place along a main controlling structure, such as a detachment or large-offset normal fault, its transport direction, that is, the direction of the main fault offset, defines the polarity of the extensional system and the major asymmetry that controls the resulting basin infill (e.g., Lister et al., 1986).

The initial dip direction of an inherited suture zone defines the subsequent extensional polarity of the asymmetric sedimentary basin system and thus the ultimate orientation of the lower and upper plate margins

after continental breakup. In this situation, faulting is controlled by simple shear mechanics (Lister et al., 1986; Wernicke, 1985) or similar mechanisms with isostatic compensation at crustal to sublithospheric scale, which create complex structures of tilted crustal blocks, detachments, core complexes, or extensional allochthons (Buck, 1988; Faccenna et al., 2014; Huet et al., 2011; Le Pourhiet et al., 2004). Such structures have been observed and modeled to be buried beneath passive continental margins such as the Newfoundland-Iberia conjugate margin, extensional back-arc areas such as the Rhodope-Aegean or Pannonian systems, or reconstructed in the evolution of mountain chains such as the Alps. In these areas dynamic scenarios of asymmetric stretching, thinning, hyperextension, exhumation, and transitions from rifting to drifting have been envisaged (Balázs et al., 2017; Crosby et al., 2011; Huismans & Beaumont, 2011; Lavier & Manatschal, 2006; Liao & Gerya, 2015; Manatschal, 2004; Manatschal et al., 2015; Péron-Pinvidic et al., 2015).

High-resolution geological and geophysical data show significant changes in along-strike geometries of rift zones (Allken et al., 2012; Chorowicz, 1989; Morley et al., 1990; Savva et al., 2014), such as changes in the major tectonic transport direction during rifting, which are in fact along-strike extensional polarity changes, that is, a lateral polarity change from an upper to a lower plate controlled by detachment faults with opposing dip directions (Lister et al., 1986; Péron-Pinvidic et al., 2015). Observation and modeling studies have inferred that the transfer zone between opposite extensional polarities accommodates complex transcurrent and distributed transtensional and extensional structures, often with en-échelon geometries, or such zones accommodate large strike-slip offsets (e.g., Corti, 2008; Lister et al., 1986; Michon & Sokoutis, 2005; Zwaan et al., 2016). Strike-slip zones are characterized by kinematic switches (changes from dextral to sinistral or the opposite). These zones change the location of the maximum crustal stretching and associated subsidence during rifting or at the onset of drifting. Such observations are available, for instance, in the Mid-Hungarian Fault Zone during the Miocene extension of the Pannonian Basin, the Paleogene-Miocene variability of the extension in the South China Sea, or the Mesozoic evolution of the Romanche Fault and its lateral prolongation in the African margin (Antobreh et al., 2009; Csontos & Nagymarosy, 1998; Fodor et al., 1998; Franke et al., 2014; Savva et al., 2014; Searle et al., 1994; Ustaszewski et al., 2008). Much less is known on the relationship between changing the sense of shear in extensional (or transtensional) transfer zones and inherited contractional polarity changes, that is, changes in the subduction dip or nappe emplacement direction along the strike of an inherited orogenic system. This polarity change is, for instance, inferred to have existed at the onset of the Pannonian Basin extension in the transition between the Alps and the Dinarides (Figure 1a), or in other orogenic or back-arc systems, such as New Guinea-New Britain, Taiwan, New Zealand, South China Sea, or the Black Sea (e.g., Csontos & Vörös, 2004; Luth et al., 2010; Metcalfe, 2002; Molli & Malavieille, 2011; Munteanu et al., 2014; Ustaszewski et al., 2008).

In this study, we conduct a series of 3-D thermomechanical numerical experiments to investigate the influence of inherited rheological weak zones and contractional polarity changes during the subsequent continental rifting and the formation of extensional basins and continental passive margins. We analyze the geometry of extensional structures, together with the subsidence and thermal evolution of an initially hot crust and thick lithosphere that contains one or two weak zones with opposite dip directions. The modeling results are discussed in a reference model followed by a parametrical study of subsequent models. These results are furthermore compared with observations from the Neogene Pannonian Basin of Central Europe.

2. Methodology

The model is based on the thermomechanical code I3VIS (Gerya, 2010a, 2013a), which solves the mass, momentum, and energy conservation equations for incompressible media. Physical properties are transported by Lagrangian markers that move with the velocity field interpolated from the fix grid. The code uses non-Newtonian viscoplastic rheologies (Table 1) to simulate multiphase flow and is specifically designed to study dynamic processes during lithospheric extension.

2.1. Thermomechanical Model

The numerical algorithm, based on staggered finite differences and marker-in-cell techniques, solves the mass (1), momentum (2), and energy conservation (3) equations for incompressible media:

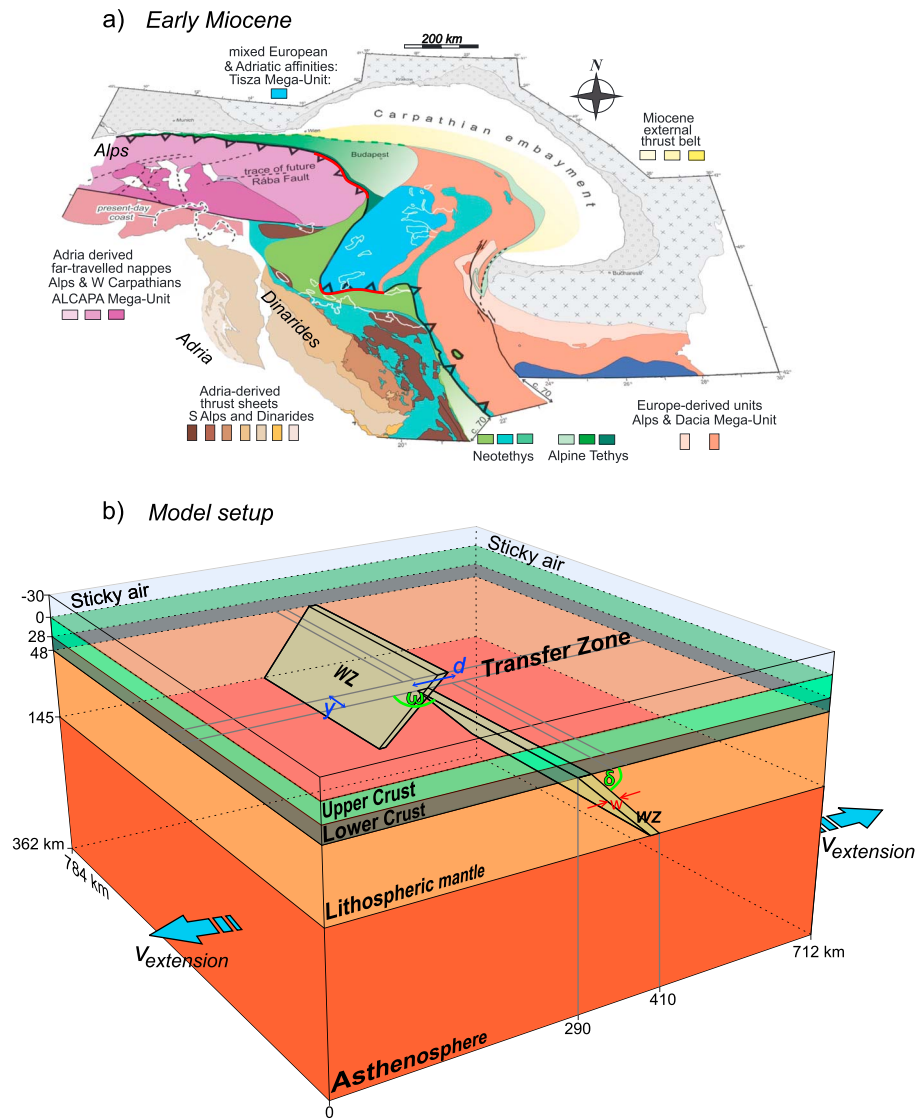


Figure 1. (a) Early Miocene reconstruction of the Alpine-Carpathian-Dinaridic system prior to the extension of the Pannonian Basin (modified after Ustaszewski et al., 2008). Note the opposing subduction and suture polarities along the Alpine and Dinaridic units. The red lines indicate the suture segments that were favorable for Miocene reactivation. (b) Initial setup of our 3-D numerical modeling. Location of the weak zones in the lithosphere represents the Neotethys and Alpine Tethys suture zones. The blue arrows indicate constant extensional boundary velocities. Further model setup parameters are listed in Table 1.

$$\frac{\partial v_i}{\partial x_i} = 0 \quad (1)$$

$$\frac{\partial \sigma_{ij}}{\partial x_j} - \frac{\partial P_i}{\partial x_i} = -\rho g_i \quad (2)$$

$$\rho C_{p,eff} \frac{DT}{Dt} = \frac{\partial}{\partial x_i} \left(k \frac{\partial T}{\partial x_i} \right) + H_r + H_s + H_a \quad (3)$$

$$H_a = T\alpha \frac{DP}{Dt} \quad (4)$$

$$\rho_{T,P} = \rho_0 (1 - \alpha(T - T_0)) (1 + \beta_c(P - P_0)) \quad (5)$$

Table 1
Rheological and Geometrical Parameters of the 12 Modeled Scenarios

Horizontal model dimension	712 km × 784 km				
Vertical model dimension	392 km				
Total extension velocity	2 cm/yr				
Temperature at the base of the lithosphere	1,300 °C				
Heat capacity, C_p (J/kg K)	1,000				
Thermal expansion, α (1/K)	3×10^{-5}				
Coefficient of compressibility, β_c (1/Pa)	10^{-11}				
	Upper crust	Lower crust	Mantle	Weak zone	
Thickness (km)	28	20	97	-	
Rheology	Wet quartzite	Diabase	Dry olivine	Wet olivine	
Density, ρ_0 (kg m^{-3})	2,700	2,900	3,330	3,200	
Preexponential factor, $1/A_D$ ($\text{Pa}^n \text{ s}$)	1.97×10^{17}	1.26×10^{24}	3.98×10^{16}	5.0×10^{20}	
Activation energy, E (kJ mol^{-1})	154	260	532	470	
Power law exponent, n	2.3	3.4	3.5	4.0	
Cohesion (Pa)	$1 \times 10^{7-6}$	$1 \times 10^{7-6}$	$1 \times 10^{7-6}$	3×10^6	
Coefficient of friction, $\sin(\varphi)$	0.4–0.2	0.4–0.2	0.6–0.3	0.1–0.05	
Radioactive heat production, H_r ($\mu\text{W/m}^3$)	1.8	0.18	0.022	0.022	
Thermal conductivity k (W/m/K) at T [K] and p [MPa]	$(0.64 + 807/(T + 77)) \times \exp(0.00004 p)$	$(1.18 + 474/(T + 77)) \times \exp(0.00004 p)$	$(0.73 + 1,293/(T + 77)) \times \exp(1 + 0.00004 p)$	$(0.73 + 1,293/(T + 77)) \times \exp(1 + 0.00004 p)$	
Experiment	WZ dip angle, δ	WZ thickness, w	Strike-perpendicular distance, d	Along-strike distance, y	Horizontal angle, ω
M1	40°	20 km	-	-	90°
M1rot	40°	20 km	-	-	105°
M2	40°, -40°	20 km	76 km	34 km	90°, 90°
M2thin	40°, -40°	12 km	76 km	34 km	90°, 90°
M2thick	40°, -40°	30 km	76 km	34 km	90°, 90°
M2rot	40°, -40°	20 km	76 km	34 km	105°, 90°
Mdt	65°, -40°	20 km	76 km	34 km	90°, 90°
Mrev	-40°, 40°	20 km	76 km	34 km	270°, 270°
Moffs	40°, -40°	20 km	160 km	34 km	90°, 90°
Mya	40°, -40°	20 km	160 km	84 km	90°, 90°
Myb	40°, -40°	20 km	160 km	190 km	90°, 90°
Myc	40°, -40°	20 km	160 km	250 km	90°, 90°

Note. Rheological parameters are adapted from similar numerical experiments (see details in Ranalli, 1995; Turcotte & Schubert, 2002). Cohesion is decreased due to plastic strain weakening. In the thermal conductivity equation T = temperature (K), p = pressure (MPa). For further description of model parameters see Liao and Gerya (2015).

where v is velocity; σ is the deviatoric stress tensor; P is the total pressure (mean normal stress); ρ is the density; g is the gravitational acceleration; $C_{p, \text{eff}}$ is the effective isobaric heat capacity; T is the temperature; k is the thermal conductivity, which depends on pressure, temperature, and rock composition; H_r is radioactive heating that is constant for a given rock composition (Table 1); H_s is shear heating (product of deviatoric stress and strain rate); H_a is the adiabatic heating (see equation (4)); η_{eff} is the effective viscosity for nonlinear viscoplastic deformation; α is the thermal expansion; and β_c is the coefficient of compressibility. Melting and related density and latent heat effects have been implemented using batch melting models for both mantle and crustal rocks (for details see Gerya, 2013b). The temperature equation is solved in Lagrangian form, and temperature advection is implemented through a marker-in-cell technique. The Einstein notation is used for the indexes i and j , which denote spatial directions $i = (x, y, z)$ and $j = (x, y, z)$ in 3-D.

Diffusion and dislocation creep flow laws combined with the Drucker-Prager yield criterion (e.g., Ranalli, 1995) were used to determine whether viscous or plastic deformation occurs. These are implemented in

the models and accounts for viscoplastic behavior. The effective creep viscosity η of a material is determined as follows:

$$\frac{1}{\eta_{\text{eff}}} = \frac{1}{\eta_{\text{diff}}} + \frac{1}{\eta_{\text{disl}}} \quad (6)$$

where η_{diff} and η_{disl} are calculated by using Newtonian diffusion creep and power law dislocation creep, respectively:

$$\eta_{\text{diff}} = \frac{1}{2} A_D^{-1} \sigma_{\text{crit}}^{1-n} \exp\left(\frac{PV_a + E}{RT}\right) \quad (7)$$

$$\eta_{\text{disl}} = \frac{1}{2} A_D^{1/n} \dot{\epsilon}_{\text{II}}^{(1-n)/n} \exp\left(\frac{PV_a + E}{nRT}\right) \quad (8)$$

where A_D is the preexponential factor, n is the power law exponent, V_a is the activation volume, E is the activation energy, R is the universal gas constant, $\sigma_{\text{crit}} = 10$ kPa is the transition stress from diffusion to dislocation creep (Turcotte & Schubert, 2002), and $\dot{\epsilon}_{\text{II}}$ is the second invariant of strain rate. Plasticity is implemented using the following yield criterion $\sigma_{\text{II}} \leq \sigma_{\text{yield}}$, which limits creep viscosity, altogether yielding an effective viscosity limit:

$$\eta_{\text{eff}} \leq \frac{\sigma_{\text{yield}}}{2\dot{\epsilon}_{\text{II}}} = \frac{C_0 + P_e \sin\varphi}{2\dot{\epsilon}_{\text{II}}} \quad (9)$$

where C_0 is the cohesion, φ is the friction angle, P_e is the effective pressure (total pressure subtracting the hydrostatic fluid pressure), and $\dot{\epsilon}_{\text{II}}$ is the second invariant of strain rate (for details see Gerya, 2013a). Plastic strain weakening is implemented by linearly decreasing the cohesion and friction angle over the strain interval of 0–1. Finally, Peierls creep takes over dislocation creep at sufficient high stress and low temperature ($\sigma_{\text{II}} > 200$ MPa, $T < 1,100^\circ\text{C}$), leading to the following equation (Katayama & Karato, 2008):

$$\dot{\epsilon}_{\text{II}Pei} = A_{Pei} \sigma_{\text{II}}^2 \exp\left\{-\frac{PV_a + E}{RT} \left[1 - \left(\frac{\sigma_{\text{II}}}{\sigma_{Pei}}\right)^m\right]^{n_{Pei}}\right\} \quad (10)$$

where $\sigma_{Pei} = 9.1 \times 10^9$ Pa, $A_{Pei} = 6.3 \times 10^{-5}$ Pa⁻² s⁻¹, $m = 1$, and $n_{Pei} = 2$. Effective viscosity is therefore limited by $\eta \leq \frac{\sigma_{\text{II}}}{2\dot{\epsilon}_{\text{II}Pei}}$.

Partial melting of the mantle is modeled by using the common parameterization of batch mantle melting processes of Katz et al. (2003). Lagrangian markers track the amount of melt extracted during each time step. Melting products are transported instantaneously to the bottom of the magma chamber that grows spontaneously in the shallowest region of the partially molten mantle (Gerya, 2013a). A detailed description of the modeling procedure is also available in previous studies (e.g., Gerya, 2013a; Gerya & Yuen, 2007; Liao & Gerya, 2014, 2015).

2.2. Model Setup

The 3-D setup (Figure 1b) is characterized by a volume of $712 \times 784 \times 392$ km³ with a resolution of $357 \times 197 \times 197$ nodal points. The front and back sides of the model are free slip. A 30-km-thick sticky air layer is imposed in the upper part of the volume ($\rho = 1$ kg/m³, $\eta = 10^{18}$ Pa × s, $k = 200$ W/m/K), which mimics the upper surface of the crust as a free surface (Cramer et al., 2012). A constant divergent velocity simulating extension is applied on the entire left and right boundaries of the modeled volume. During extension, compensating material enters through the upper and lower boundaries at velocities calculated by satisfying the mass conservation equation. A constant temperature boundary condition is used for these upper and lower boundaries, and thermal isolation (i.e., zero heat flux) is imposed for the lateral boundaries. The initial temperature field is horizontally uniform, and the temperature increases linearly from 0 °C at the surface to 700 °C at Moho depth (i.e., a hot continental crust), and finally to 1,300 °C at the base of lithosphere. An adiabatic temperature gradient of 0.5 °C/km is prescribed in the asthenospheric mantle. The experiments with a thick crust and lithosphere (48 and 145 km thick, respectively) simulate an orogenic area at the onset of extension. The setup contains 28-km-thick wet quartzite and 20-km-thick diabase rheology for the upper and lower crusts, respectively. The mantle lithosphere is simulated by dry olivine rheology.

2.3. Model Limitations

Our 3-D setup includes only the lithosphere and uppermost asthenosphere. Therefore, deeper mantle processes, such as subduction dynamics or further asthenospheric flow systems, are not taken into account. Uniform extensional boundary velocities were imposed on the model boundaries. Therefore, differential extension and different plate velocities are not simulated in our models. However, temporal variation of plate velocities in natural examples creates slower and faster episodes of extension and contraction (e.g., Faccenna et al., 2014). Postrift basin evolution, surface processes, and the role of different initial suture zone dip angles are investigated in previous 2-D experiments (e.g., Balázs et al., 2017). Our modeling scenario is also limited by constant prerift topography and zero initial water depth. Furthermore, our initial setup contained a laterally homogeneous crust, which assumes that other inherited thrust contacts may provide less significant rheological influence at our applied resolution.

2.4. Modeling Scenarios

The experiments are specifically designed to simulate the fast extension (2 cm/yr) of a region that contains inclined rheological weak zones located in the mantle lithosphere (Figure 1b), which resemble suture zones or major nappe contacts inherited from predated orogenic deformation. We implemented that the major rheological contrast of a suture zone is located in the lithospheric mantle due to the presence of fluids released during former subduction (Dunbar & Sawyer, 1988). This geometry and the rheology of one inherited weak zone were defined and are similar to previous 2-D modeling studies (e.g., Balázs et al., 2017; Liao & Gerya, 2014). Starting from these available models, we have defined the 3-D modeling setup of a reference model that contains two 20-km-wide and 40° inclined rheological weak zones, whose strike is perpendicular to the direction of extension, and they have opposite dip directions (model M2, Figure 1b). These weak zones are simulated by wet olivine rheology with low friction angle value (Table 1) and have an initial 76-km strike-perpendicular and 34-km along-strike offset from each other (d and y in Figure 1b). This initial configuration resembles a former contractional polarity change (Munteanu et al., 2014) of an inherited orogenic area. The weak material that initially defines the suture zones becomes advected and deformed during the model simulations, which has important consequences on the pattern of faulting and lithospheric thinning.

Parameter tests on the influence of extension velocities, sedimentation and erosion rates, initial weak zone dip angles, and initial crustal and lithospheric thicknesses are already available in previous studies (Balázs et al., 2017). In this study we subsequently focus on the 3-D influence of these geometrical and compositional parameters and their along-strike interaction during extension (Table 1). We show modeling results with variable dip angle of the lithospheric weak zones (δ in Figure 1b), across and along-strike offsets between the weak zones (d and y in Figure 1b), the absence of one of the two weak zones (i.e., models with just one inclined weak zone), the angle of obliquity between the strike of the weak zones, and the direction of extension (ω in Figure 1b). We furthermore test the influence of different initial weak zone width values (w in Figure 1a). Numerical modeling results are illustrated by the evolution of subsidence and topography (Figure 2), effective viscosity (Figures 2–7 and 10), crustal and mantle layering geometries (Figures 2–7 and 9 and 10), and strain rate distribution (Figures 9 and 10). Furthermore, crustal and lithospheric mantle thinning factors (β and γ) were calculated along 2-D sections (Figures 8 and 9) based on the ratio of the initial and final crustal and lithospheric mantle thicknesses, respectively.

The nomenclature of extensional transfer zone is fairly complex by using the kinematics and type of faults modeled or observed in nature. Previous studies have differentiated for instance oblique linkage zones where continuous deformation connect different rift segments, step overs, and bend overs where an offset is observed between parallel rift segments, or transfer strike-slip where a fault with perpendicular strike offsets the rift segments (Allken et al., 2012; Brune et al., 2017; Corti, 2009; Zwaan et al., 2016). Such detailed features are beyond the resolution of our models in transfer zones, and therefore, we have chosen to adopt a simpler terminology by describing step overs (either dextral or sinistral) connecting rift segments and oblique faults or shear zones (normal-dextral or normal-sinistral) where the offset deviates from the dip-slip kinematic direction.

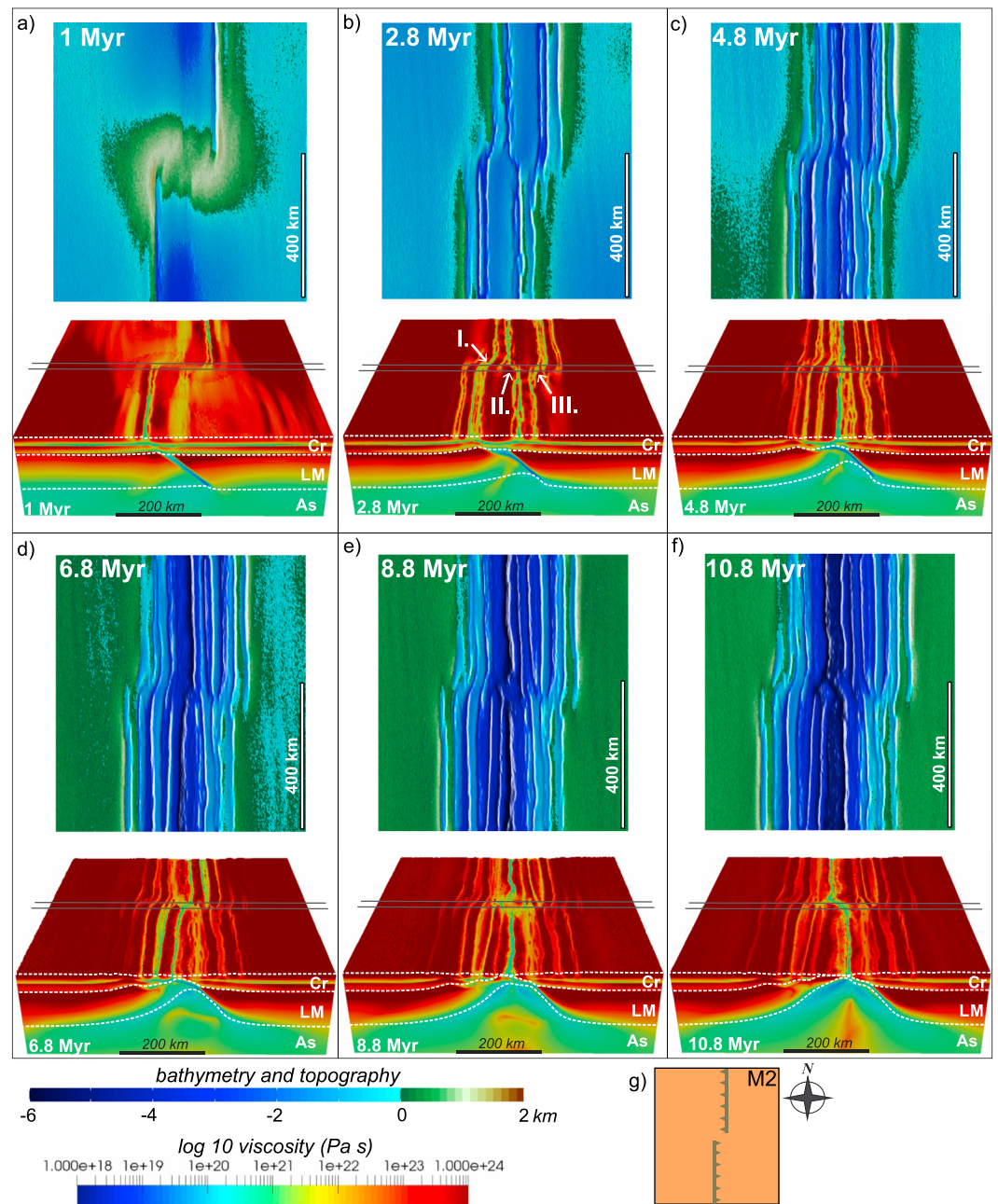


Figure 2. (a–f) Evolutionary model of the experiment with two oppositely dipping inclined weak zones (M2) shown by the (top row) topography and bathymetry and (bottom row) effective viscosity results. The gray lines in the viscosity figures indicate the horizontal boundary of the oppositely dipping weak zones corresponding to the transfer zone location (see Figure 1b). Note the three step over structures in Figure 2b (I–III). Cr, crust; LM, lithospheric mantle; As, asthenosphere. (g) Top view sketch showing the initial weak zone geometry applied in our numerical model.

3. Model Results

3.1. The Reference Model Containing Two Oppositely Dipping Weak Zones

At the onset of extension, deformation localizes along and at the upper boundary of the lithospheric weak zones (Figure 2a). This deformation is associated with conjugate low offset normal faults dipping in the opposite direction to the weak zone. This geometry creates an asymmetric depression in the hanging wall that is associated with ~1-km uplift in the footwall of the main fault formed above both weak zones (see topography panel in Figure 2a). These normal faults are perpendicular to the extensional direction and are not connected

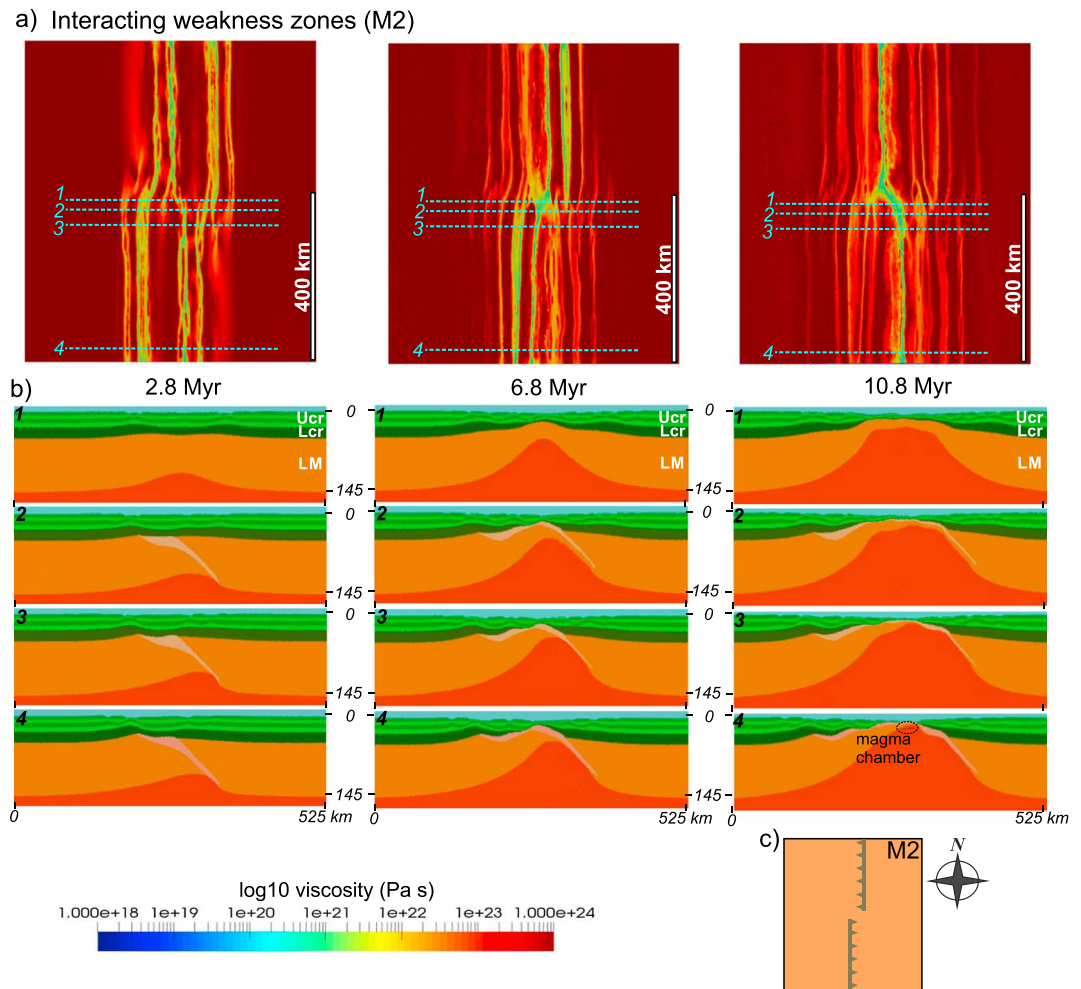


Figure 3. Evolution of crustal and lithospheric layering of the reference model (model M2) at three different time steps. (a) Effective viscosity maps highlight zones of active deformation. (b) 2-D vertical cross sections (1–4) show the crustal and lithospheric evolution at different times. Three sections are located inside and in the vicinity of the transfer zone (1–3), while one section (4) is located at larger distance (~300 km) from this transfer zone. Note the symmetric structures in the transfer zone (sections 1–3) and asymmetric crustal geometries above the weak zones (section 4). Ucr, upper crust; Lcr, lower crust; LM, lithospheric mantle. (c) Top view sketch showing the initial weak zone geometry applied in our numerical model.

in the central area of the model, where crustal deformation is initially distributed over a wide area during the first ~1.5 Myr of extension and creates an initial elevated topography (Figure 2a). Fast asymmetric asthenosphere upwelling is associated with advective redistribution of lithospheric mantle weak zones beneath the crust, which localizes deformation along multiple fault systems (Figures 2b–2f and 3). As extension progresses, fault segments in the transfer zone connect by creating three step overs, two dextral (I and III) and one sinistral (II in Figure 2b). The center of the transfer zone displays a symmetric structure flanked by equally spaced (half-) graben on both sides (section 1 in Figure 3b), while the structure at farther distance from the center of the model becomes gradually more asymmetric, where the largest fault offset is located in the place where the displacement along the weak zone shears the (upper) crust (sections 2–4 in Figure 3b).

The continuation of the extension is characterized by the gradual opening of new half-grabens above the weak zone that is redistributed at the base of the crust (Figures 2b–2e). At 6.8 Myr after the onset of extension, the maximum subsidence in the transfer zone is accommodated by a dextral step over connecting the central half-grabens (Figure 2d). At this time, the overall deformation is characterized by marked asymmetry and by shearing of the entire lower crust in areas recording large amounts of thinning (Figure 3b).

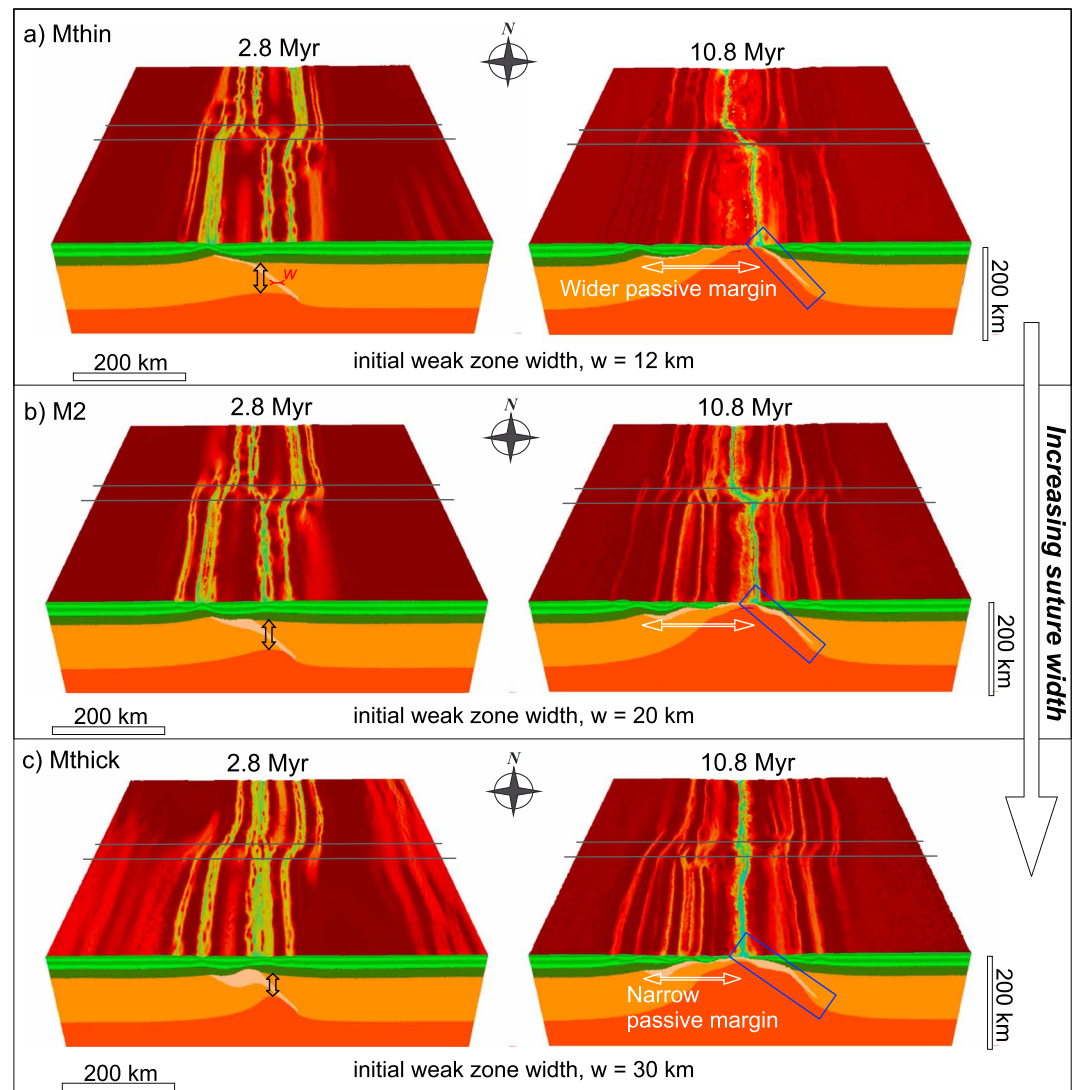


Figure 4. Influence of different initial weak zone width values (12, 20, and 30 km) shown by effective viscosity in top view and phase configuration in vertical cross section. Same scale is applied as in Figure 2. Note that a larger initial suture width creates a more symmetrical and faster crustal and lithospheric thinning leading to lower horizontal offset between the active rift segments at the end of the modeling at 10.8 Myr. A larger initial weak zone width also leads to a narrower footwall passive margin (indicated by white horizontal arrow measured from the initial location of the suture) and a more gently dipping lithosphere-asthenosphere boundary at the remnant of the suture (indicated by blue rectangle).

At 8.8 Myr after the onset of extension, the deformation localizes in the model center, while minor distributed deformation occurs laterally (Figure 2e). At ~10.8 Myr after the onset of extension, the maximum subsidence in the transfer zone is accommodated by a sinistral step over or prototransform fault (Gerya, 2010b) due to opposite transport directions during extension (Figure 2f). Earlier formed half-grabens remain inactive and are distributed laterally over a wide area. This distribution is symmetric in the transfer zone (section 1 at 10.8 Myr, Figure 3b) and becomes highly asymmetric at farther distances. Significantly tilted normal faults with largely uplifted footwalls overlying highly thinned or absent lower crust are observed over the redistributed weak zone and its uplifted mantle lithosphere footwall (sections 2–4 at 10.8 Myr, Figure 3b). In contrast, the part of the model that evolved in the hanging wall of the weak zone shows lower offset normal faults and lower amounts of lower crustal thinning. Partial melting is generated beneath the lithosphere-asthenosphere boundary after ~10 Myr at far distances from the transfer zone (section 4 in 10.8 Myr, Figure 3b). The reference model development suggests that the initial weak zones impose very strong controls on the evolution serving as two long-living detachment faults in the mantle, which sustain

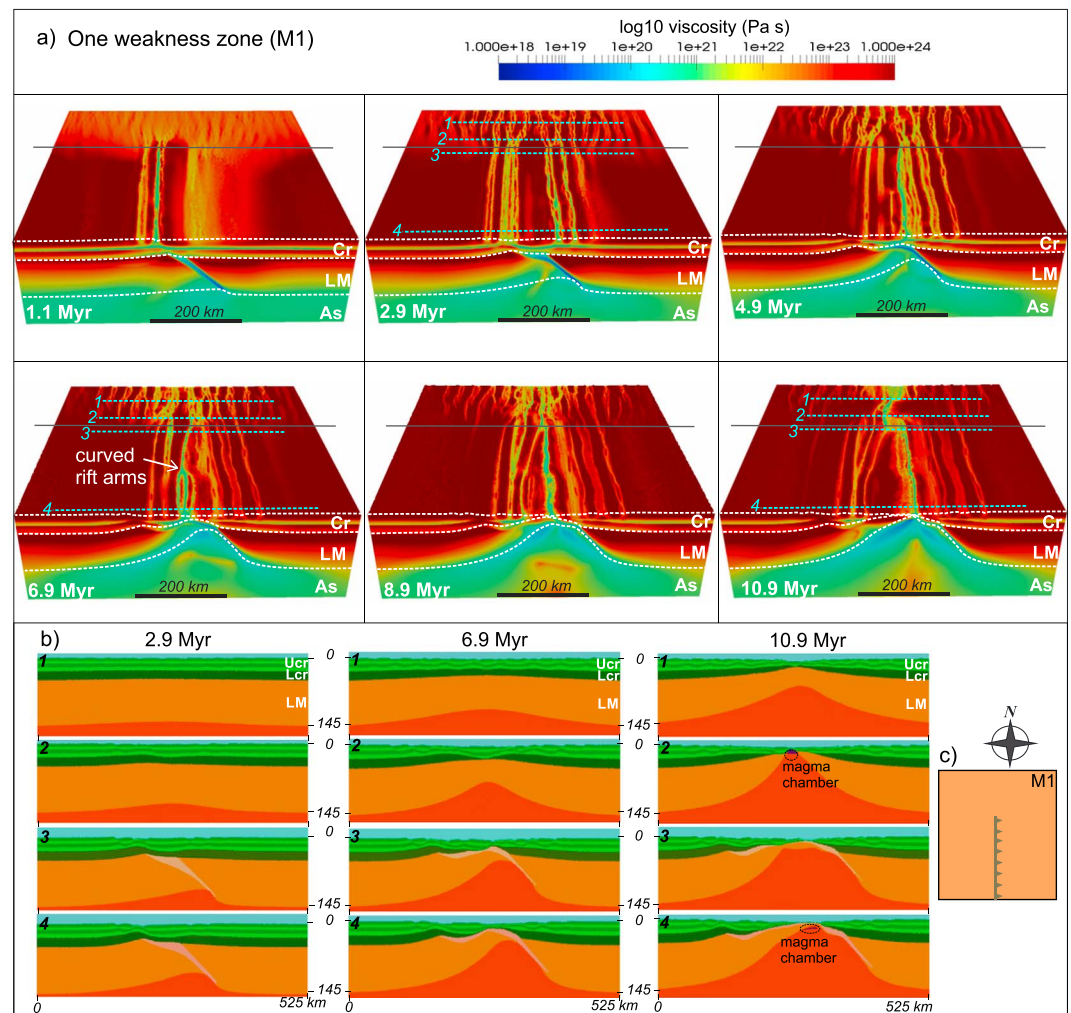


Figure 5. Evolutionary model of the experiment with one weak zone (model M1). (a) Effective viscosity results highlighting the zones of active deformation. The gray line indicates the horizontal boundary of the weak zone located in the lithosphere. (b) 2-D vertical cross sections show the crustal and lithospheric evolution at different times along the sections (1–4). Note the asymmetric crustal geometries above the weak zone (sections 3 and 4) and the distributed overall more symmetrical crustal and lithospheric geometries in the model area without a weak zone (sections 1 and 2). Cr, crust; Ucr, upper crust; Lcr, lower crust; LM, lithospheric mantle; As, asthenosphere. (c) Top view sketch showing the initial weak zone geometry applied in our numerical model.

until the onset of the oceanic spreading. Opposite polarity of these faults causes their migration toward each other by asymmetric mantle lithosphere extension and thermal accretion. As the result, these detachment faults pass each other during rifting and create a growing sinistral prototransform zone connecting them. A similar phenomenon of ridge offset change has been documented in models of transform evolution at slow spreading ridges (Püthe & Gerya, 2013).

3.2. Parametric Study

The effect of different initial weak zone width (12, 20, and 30 km) are modeled in three scenarios (Figure 4), where all other parameters are kept identical to the reference model. A larger initial suture width creates a more symmetrical crustal and lithospheric thinning that leads to a lower horizontal offset between the active rift segments at the end of modeling. A larger initial weak zone width also leads to a narrower passive margin (in the footwall of the weak zone), a thinner lithosphere below, and a more gently dipping lithosphere-asthenosphere boundary along the segment of the suture zone dipping in the mantle (Figure 4).

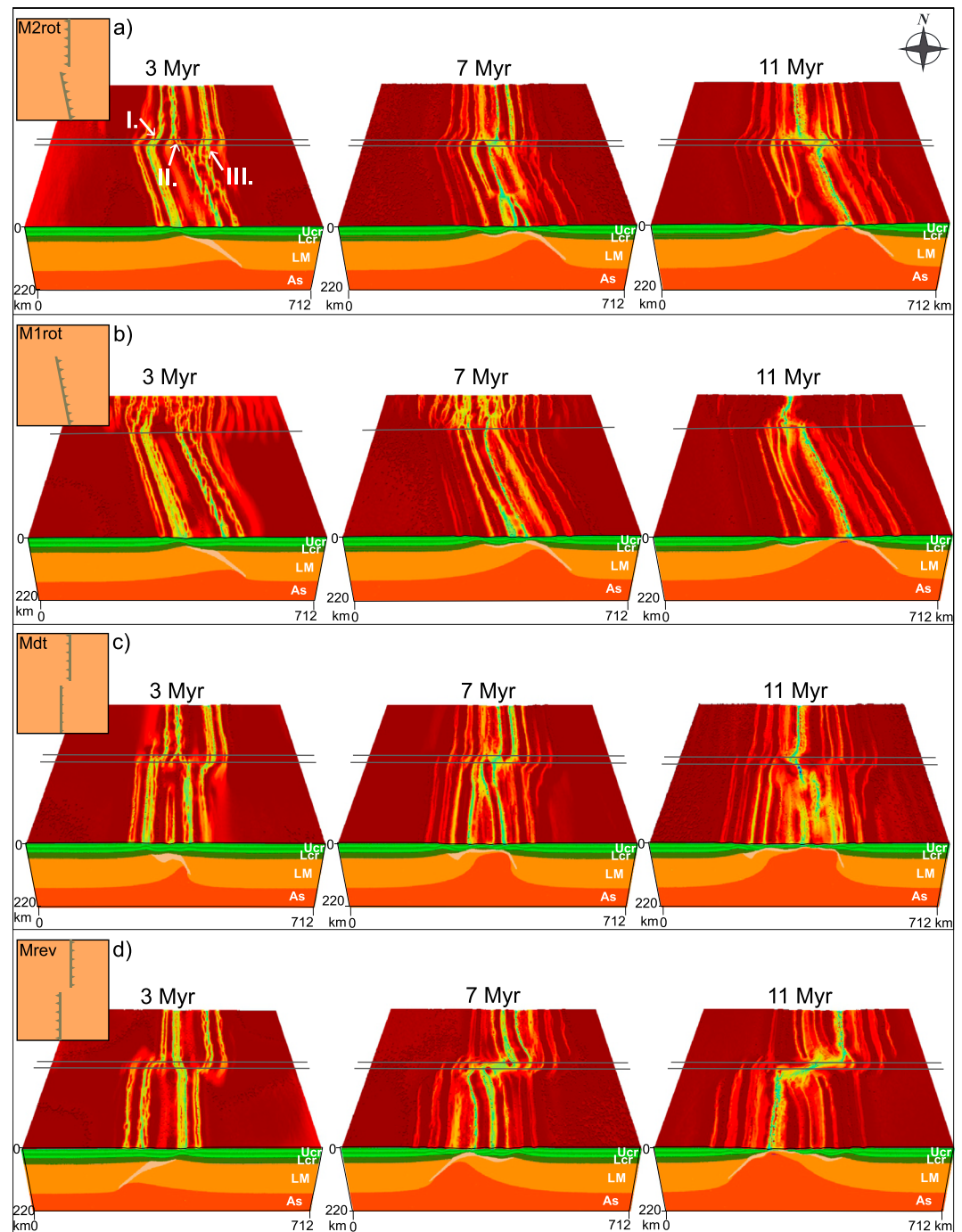


Figure 6. Influence of different initial weak zone geometries shown by effective viscosity in top view and phase configuration in vertical cross sections. Same scale is applied as in Figure 2. Ucr, upper crust; Lcr, lower crust; LM, lithospheric mantle; As, asthenosphere. (a) M2rot, one of the weak zones is oblique. (b) M1rot, model with one oblique weak zone. (c) Mdt, one of the two weak zones has an initial steeper dip angle. (d) Mrev, reversed initial weak zone dip angles. The gray lines in the viscosity figures indicate the horizontal boundary of the weak zones corresponding to the transfer zone locations.

The model with one weak zone (model M1, Table 1; see also the supporting information file) simulates the lateral transition to an area where such types of weakness are not present (Figure 5). The part of the model containing the weak zone shows an evolution characterized by marked asymmetry associated with localized deformation, footwall uplift, and lower crustal thinning that are fairly similar to

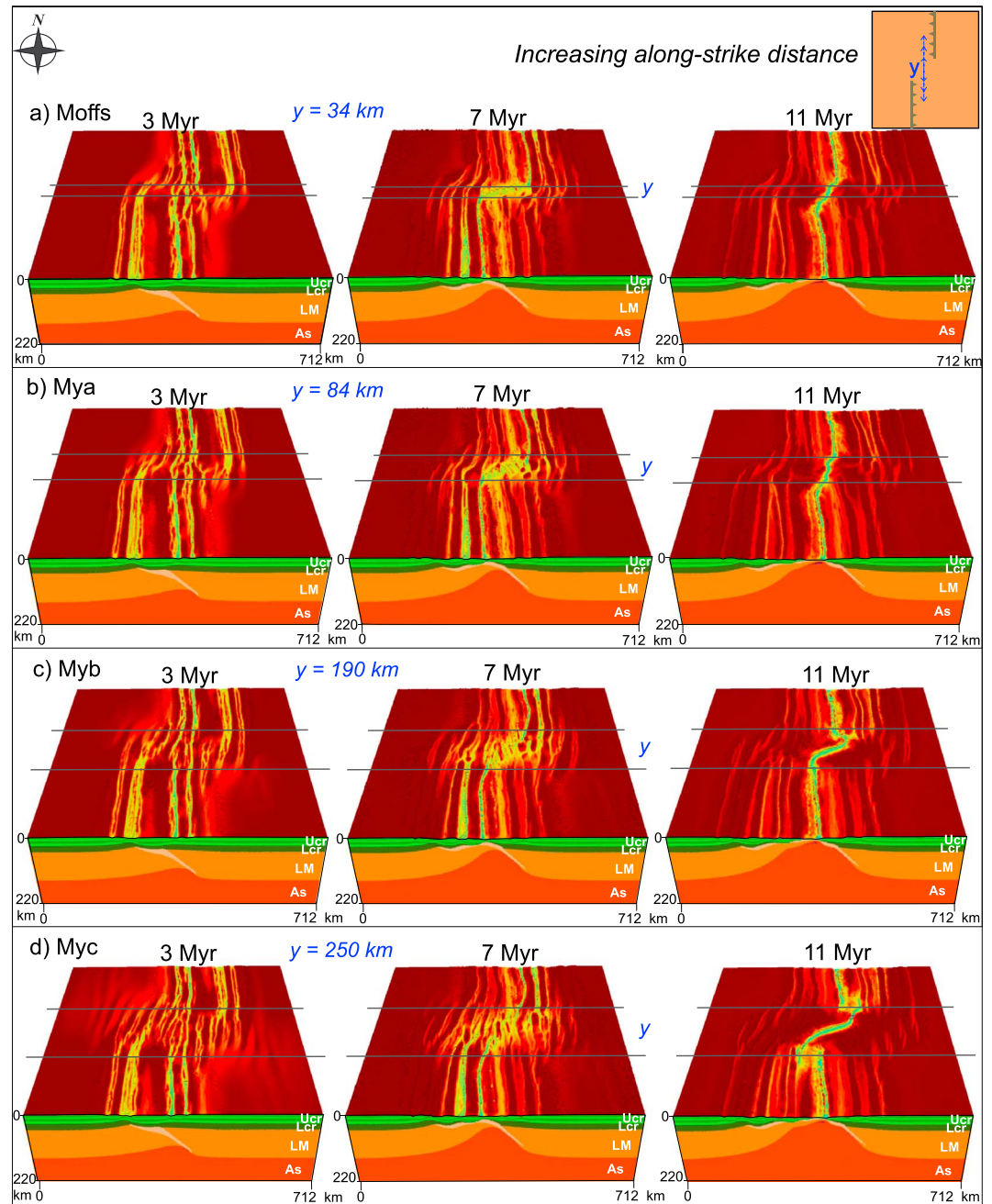


Figure 7. Influence of different along-strike distances (34, 84, 190, and 250 km) between the weak zones. Results are shown by effective viscosity in top view and phase configuration in vertical cross sections. Same scale is applied as in Figure 2. Ucr, upper crust; Lcr, lower crust; LM, lithospheric mantle; As, asthenosphere. The gray lines in the viscosity figures indicate the horizontal boundary of the weak zones corresponding to the transfer zone locations.

the reference model with two weak zones (compare section 4 in Figures 3b and 5b). The part of the model without a weak zone shows at first (Figure 5a) a wide zone of deformation in the entire model, followed by gradual localization in its center and the formation of a symmetric structure (section 1 in Figure 5b). Structures become more localized and asymmetric toward the location of the weak zone (compare sections 2–4 in Figure 5b). Localized rift segments in the area overlying the weak zone mechanically interact with the symmetric distributed structures. This interaction results in the formation of sinistral and dextral step overs (Figure 5a). The difference between the symmetric

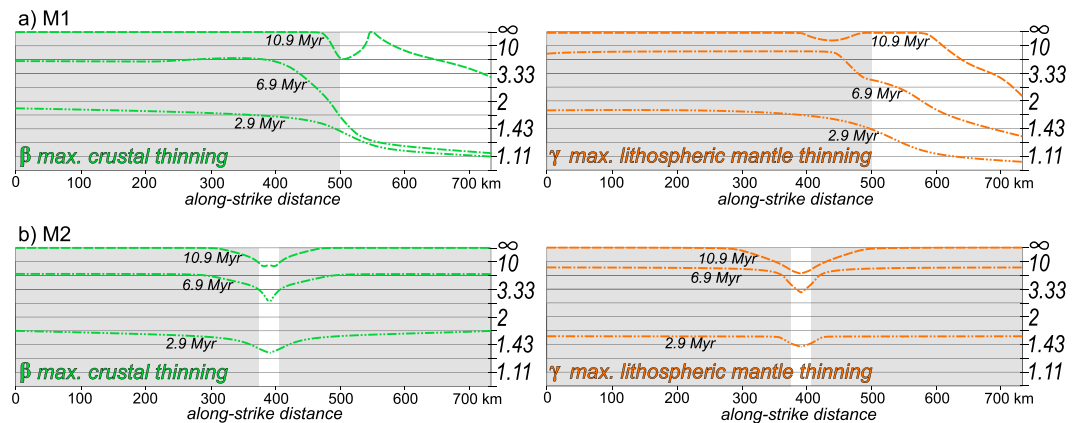


Figure 8. The evolution of the maximum crustal and lithospheric mantle thinning factors plotted parallel with the weak zone strike. Maximum thinning factors were selected from 2-D sections perpendicular to the strike of the weak zones and plotted along their strike in M1 and M2 models (one and two weak zones). The gray domain indicates the location of weak zones in the lithosphere, while the white area (offset 500–740 km in Figure 7a and offset 375–409 km in Figure 7b) corresponds to the model area where no weak zone is present.

extensional transport directions toward the center of the model and the dominant top-right transport direction in the areas without and with a weak zone, respectively, creates a large sinistral step over structure. The extreme shearing in this transfer zone induces partial melting beneath the lithosphere-asthenosphere boundary (section 2 in Figure 5b).

We have tested two modeling scenarios containing one oblique weak zone (angle between the strikes of the weak zones: $\omega = 105^\circ$, Figure 1b, models M2rot and M1rot, Table 1). In a first oblique scenario (model M2rot, Figure 6a), the model contains also one other weak zone perpendicular to the direction of extension. In this scenario, deformation follows generally the orientation of the oblique weak zone. Normal faults form above the oblique weak area. They have an en-échelon geometry and perpendicular strike to the extension direction during the first 4 Myr (3 Myr, Figure 6a). Subsequent deformation in this area localizes along oblique faults or shear zones with normal-dextral offsets, and their strike becomes parallel with the initial weak zone. These faults and shear zones are accommodated along-strike by two dextral and one sinistral step overs in the transfer zone at 3 Myr after the onset of extension (I, III, and II respectively, Figure 6a). After 7 Myr of extension the faults with oblique offset form splays with normal offset that separate and connect subbasins along their strike, while step overs in the transfer area are dominantly dextral (see also Figure S3 in the supporting information). Toward the end of the modeled extension time (11 Myr, Figure 6a), deformation localizes along one large offset fault in each of the two areas (overlying the weak zone in the south and without predefined weakness in the north, respectively) that creates a large sinistral step over.

The second scenario (model M1rot, Figure 6b) contains only the oblique weak zone with the same geometry as the previously described model (i.e., $\omega = 105^\circ$). The results are a combination between models M1 (Figure 5) and M2rot (Figure 6a). A wide zone of deformation is observed initially in the northern model area without a weak zone that gradually localizes due to the northward propagation of the shear zone initiated by the weak zone. The obliquity of the weak zone induces an initial en-échelon geometry that subsequently creates splays and subbasins oriented perpendicular to the direction of extension. Similar to the M2rot model, multiple initial dextral step overs are ultimately replaced by one sinistral step over with larger offset (compare Figures 6a and 6b).

The effects of the dip angle (δ in Figure 1b) were tested in a model by increasing this angle for the southern weak zone (Figure 6c, $\delta = 65^\circ$; Mdt, Table 1). The results show that a steeper weak zone facilitates lithospheric thinning and asthenospheric upwelling over a narrower area in comparison with previous models (compare Figures 6a and 6c). Most step overs are initially dextral, while deformation subsequently localizes in one large sinistral step over, although with a smaller offset when compared with the reference model. The higher dip

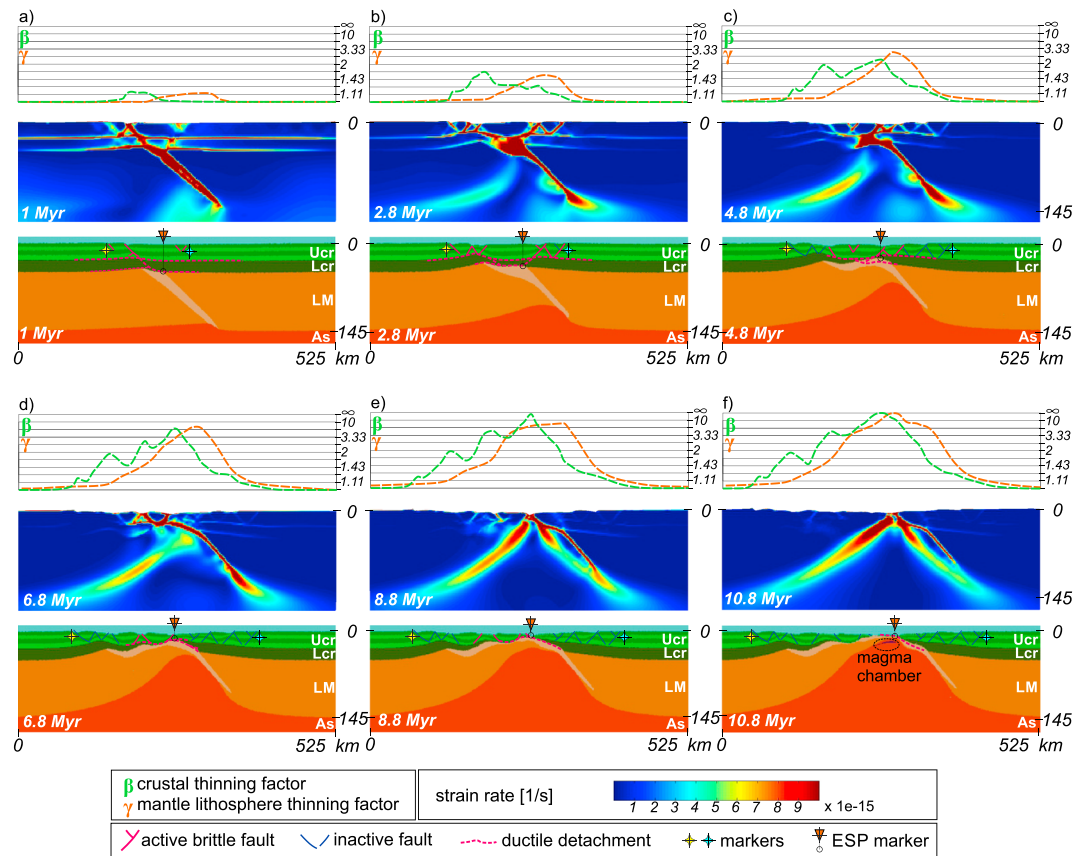


Figure 9. Interpreted structural evolutionary model of the experiment with two weak zones (model M2). Location of the 2-D section is shown in Figure 3 (section 4). (top row) Crustal and lithospheric mantle thinning values underlain by strain rate figures. (bottom row) The phase configuration of the model indicating the active and inactive structures. Two marker points are plotted at the sides of the extending domain and we defined an extensional singularity point (ESP) marker that shows the future location of breakup. ESP is projected to the surface in the figures.

angle favors a larger amount of localized lithospheric mantle shearing, reaching faster oceanic spreading (before 11 Myr in Figure 6c).

The effects of the dip direction were tested in an experiment (Mrev, Table 1), where the two weak zones dip outward, that is, in an opposite direction when compared to the reference model (compare Figure 2 with Figure 6d). The comparison with the reference model shows a similar evolution during the first ~3 Myr of extension. However, the preimposed dextral offset is subsequently accentuated by the opposite transport directions and the ultimate result is the creation of a very large dextral step over. A strike-slip duplex developed at ~7 Myr in the transfer zone (red circular areas in the transfer zone, Figure 6d). These structures are subsequently sheared and cannot be recognized in later stages of deformation.

The effects of the along-strike distance between the weak zones (y in Figure 1b) were analyzed in a series of experiments that contained four different initial y values (34, 84, 190, and 250 km, Figure 7, model Moffs, Table 1) and a constant strike-perpendicular distance between the weak zones (constant $d = 160$ km, Figure 1b). When y is the same, but d is greater than in the reference model (Figure 7a), a greater strike-slip offset is observed along step overs, while they remain dextral in the localized transfer zone at the end of the model. Increasing the along-strike distance between the weak zones results in more widely distributed deformation in the transfer zone in the initial stages of deformation, while the later deformation localizes along a large step over, whose geometry is controlled by the width of the transfer zone. The final rift architecture after 11 Myr is different in these models (Figures 7a–7d) and gradually shows a transition from an oblique continuous rift arm to a discontinuous bending transform fault.

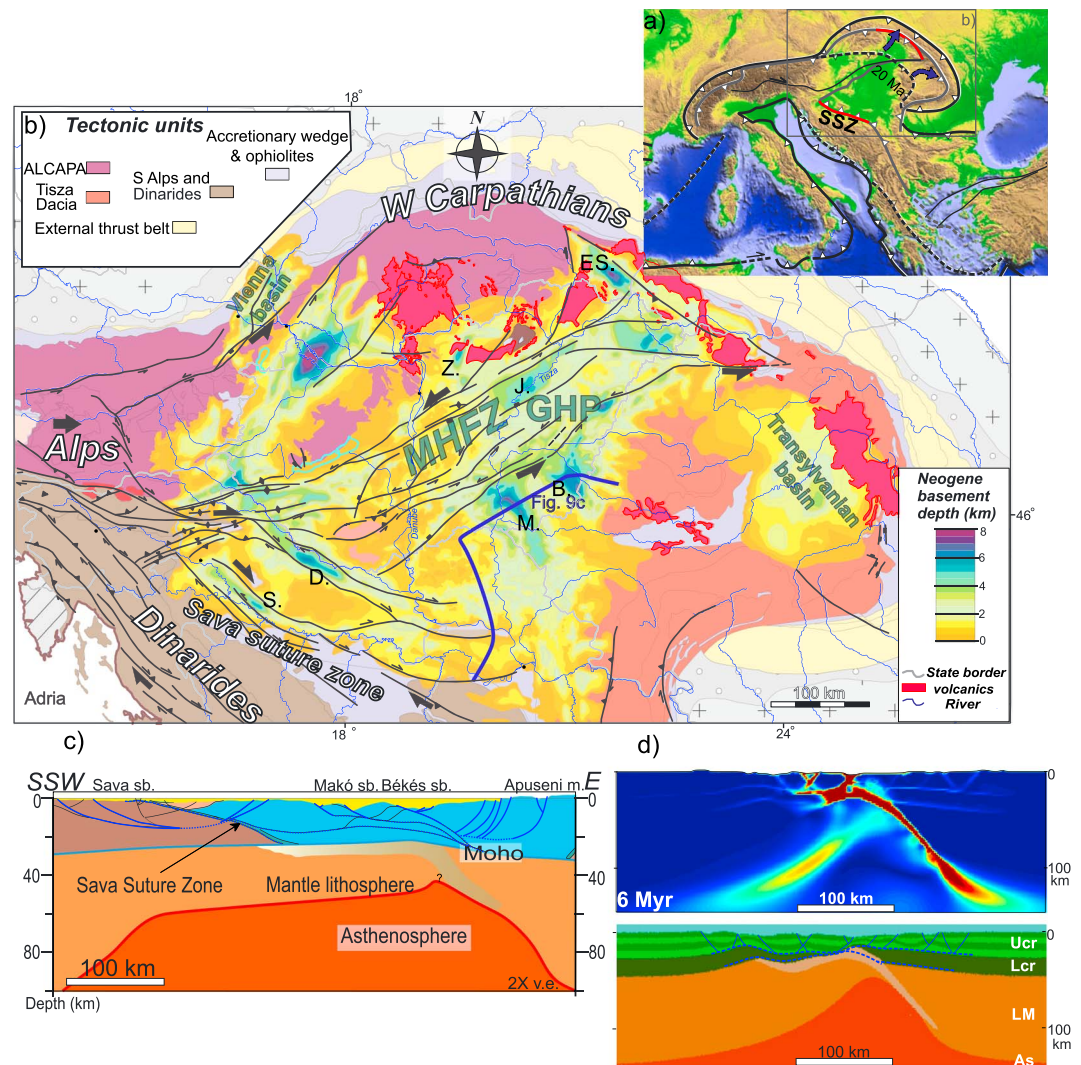


Figure 10. Comparison of our model results with the extension of the Pannonian Basin of Central Europe. (a) Simplified tectonic outline of the Alpine-Carpathian-Dinaric-Hellenic region. The black and gray lines indicate the main sutures in the region. The dashed lines show the position of the orogenic fronts prior to back-arc extension. The red lines indicate the sutures that were reactivated during extension. SSZ, Sava suture zone. (b) Neogene basement depth map overlain by the main strike-slip fault zones in the Pannonian Basin system. Note the wide transcurrent Mid-Hungarian Fault Zone in the middle of the basin. GHP, Great Hungarian Plain. Pre-Neogene basement units are restored in Figure 1a. M, Makó subbasin; B, Békés subbasin; D, Dráva subbasin; S, Sava subbasin; Z, Zagyva subbasin; ES, East Slovak Basin; J, Jászság pull-apart basin. (c) Interpreted composite section through the southern parts of the basin. Upper crustal geometry is based on seismic interpretation (cf. Balázs et al., 2017). The Sava suture zone in mapped at the Dinaridic margin and inferred at depth toward the east. (d) Numerical modeling result of the reference experiment (model M2) shown by the strain rate after 6 Myr and phase configuration. Ucr, upper crust; Lcr, lower crust; LM, lithospheric mantle; As, asthenosphere.

4. Discussion

4.1. Strain Transfer Between Weak Zones During Extension

Inherited rheological weak zones dipping in the mantle lithosphere localize extensional deformation in the form of long-living migrating lithospheric-scale detachment faults. These faults create dominantly asymmetric structures associated with rapid asthenospheric upwelling and lithospheric mantle thinning. Crustal deformation is controlled by the redistribution of weak zones beneath the Moho, which creates an effective rheological decoupling between the crust and mantle lithosphere.

The temporal evolution of crustal and lithospheric thinning (Figure 8) can be described by using the maximum thinning factor (MTF). Such thinning factors are sensitive to crustal and lithospheric mantle strain localization.

$$\beta(Y, t) = \max_x \left(\frac{Cr_0}{Cr_t} \right) \quad (11)$$

$$\gamma(Y, t) = \max_x \left(\frac{Li_0}{Li_t} \right) \quad (12)$$

Crustal and lithospheric mantle thinning factors (β and γ) were calculated and plotted along the strike of the weakness zones (Y), at different times (t) based on the strike-perpendicular selected maximum value (\max_x) of the ratio of the initial (Cr_0 and Li_0) and final (Cr_t , Li_t) crustal and lithospheric mantle thicknesses, respectively. In the model with one weak zone (Figure 8a), extensional deformation localizes rapidly along the weak zone and the in the overlying crustal area. In contrast, MTF is low in the area where no initial weak zone is present (Figure 8a). The gradual decrease of MTF toward the area without weak zone is controlled by crustal splaying and formation of individual subbasins (Figure 5). The lateral differences in shearing between the symmetric, distributed rifting in the north, and the localized asymmetric one in the southern modeling domain together with their mechanical interaction (Figure S2) create a local asthenospheric upwelling (section 2 in Figures 5b and 8). This initiates decompressional melting driven by spreading and thinning that locally weakens the lithosphere (Figure 5b), when compared with other models.

During the first ~3–5 Myr of extension MTF in the weak zone area is greater in models with one weak zone when compared with models with two zones (models M1 and M2, respectively, Figures 8a and 8b). This is because two weak zones transfer deformation in the entire model area facilitated by the transfer zone. In contrast, in the area overlying the only weak zone, deformation is more localized, resulting in greater MTF values. Lithospheric sutures, therefore, influence crustal evolution during extension in the entire model domain. MTF is initially lower in the transfer zone, where crustal deformation is distributed over a wider distance (Figure 3a). MTF subsequently increases leading to crustal breakup above the weak zones after ~11 Myr.

4.2. The Asymmetry of Extension

The crustal and mantle lithosphere thinning factors in the reference model (model M2) are shown in a cross section located at far distances from the transfer zone (Figure 9, location of section 4 in Figure 3). Crustal thinning factors indicate brittle faulting and subbasin subsidence in narrower areas, while the mantle lithospheric thinning is smoother. A lateral offset is observed between the location of the crustal and lithospheric mantle MTF. The offset is primarily controlled by the initial dip angle of the weak zone and the initial lithospheric thickness. This offset is initially large (~100 km, Figure 9a) but subsequently decreases to only few kilometers due to the gradual localization of deformation above the redistributed weak zone and gradual thinning of the initially thick lithospheric mantle (Figures 9b–9f). This evolution shows asymmetric crustal and mantle geometries, although the distance between crustal and mantle MTF gradually decreases. The pattern of extension during continental rifting is initially asymmetric but becomes more symmetric by two conjugate lithospheric shear zones before seafloor spreading occurs.

The MTF offset and the geometry of deformation are driven by the asymmetric character of extension, controlled by the uplift of mantle lithosphere in the footwall of the weak zone. This uplift and redistribution of the weak zone beneath the crust control the formation of rotated low-angle listric normal faults and their tilting, associated with the formation of detachments combined with shearing and exhumation of middle crustal layers. After 4.8 Myr of extension this exhumation reaches a maximum depth of ~14 km, while the lower crust is gradually sheared away from the basin center (Figure 9c). In contrast, the crustal deformation above the part of the weak zone still dipping in the mantle lithosphere is characterized by a series of low offset normal faults (right margins in Figures 9c–9e).

In fact, the symmetry of the system during extension is controlled by the location of the point that separates the redistributed weak zone beneath the crust and the part of the weak zone that is still dipping in the mantle. It was assumed that asymmetric extension was initiated by a lithospheric weak zone and the crust is initially, laterally homogeneous at our resolution. By analogy with orogenic models (e.g., Willett & Brandon, 2002),

we define an extensional singularity point (ESP, Figure 9). In orogenic models, this singularity point separates the zone where the crustal part of the lithosphere is accreted from the one where its mantle lithosphere is subducted (see also Beaumont et al., 2000, and references therein). In our models, ESP is located at the onset of extension at the upper tip of the weak zone and subsequently separates the zone where the mantle lithosphere is continuously exhumed toward the base of the crust from the one where the mantle lithosphere and its overlying weak zone are redistributed laterally. ESP is also the point where maximum shearing is continuously recorded at the contact between the crust and mantle lithosphere. This shearing is taken by the lower crust and transported laterally far into the footwall of the weak zone during extension. The rapid shearing, exhumation, and thinning to disappearance of the lower crust during extension reduce the MTF offset between the crust and mantle lithosphere (Figure 9). At the same time, older structures are transported laterally in the direction of the footwall. When the lower crust is completely sheared away, normal faults are rooted directly into the ESP. Transmission of deformation from the ESP upward into the crust and downward into the mantle lithosphere competes with another mechanism, the rheological decoupling between the crust and mantle lithosphere that increases gradually due to the redistribution of the weak zone beneath the crust (Figure 9). The migration of deformation laterally from the ESP creates a more symmetrical appearance of the crustal and lithospheric structures at the end of extension, prior to continental breakup, although the width of the footwall margin is ~ 125 km larger than the hanging wall one (Figure 9f). The age of the various structures and subbasins is different on both margins, younger near the ESP and older at farther distances.

The above described asymmetric extensional mechanism works when the weak zone provides major rheological contrast in the lithospheric mantle. An initially thicker weak zone creates faster lithospheric mantle thinning, and therefore, it requires less time to locally thin the entire lithosphere when compared to the experiment with a thinner weak zone (Figure 4). Faster lithospheric mantle thinning is subsequently followed by the formation of symmetrical shear zones, creating an overall symmetric asthenospheric upwelling and a narrower lower plate passive margin.

4.3. Extensional Interaction in the Transfer Zone

Our experiments show the formation of complex rift interaction zones between areas overlying rheological weak inclined zones. Similar numerical and analogue modeling studies (Allken et al., 2012; Le Pourhiet et al., 2017; Zwaan et al., 2016) highlight the importance of strong coupled or weak decoupled crustal rheologies, rheological contrasts in the mantle lithosphere, and the horizontal distance between initial rift segments. Our experiments account for a hot and therefore weak lower crust that is similar to recent orogenic areas (Tesauro et al., 2009).

Similar to previous modeling studies (Allken et al., 2012; Zwaan et al., 2016) a greater lateral distance between the interacting rift segments creates discontinuous linkage zones, where normal faults do not connect directly but create oblique step over or bend over structures. In contrast, a smaller lateral distance between the interacting rift segments creates oblique connecting pull-apart basins or strike-slip transform faults. Our key observation is the change in step over and strike-slip transfer kinematics from diffused to localized and a change between their sinistral and dextral senses of apparent shear during extension. Gradual opening of new subbasins during extension locally creates new sinistral or dextral step overs and strike-slip fault offsets that overprint previous structures in the transfer zone.

Crustal-scale models (i.e., without thermal coupling, e.g., Allken et al., 2012) inferred that a continuous rift linkage occurs when the initial horizontal distance between the rift segments is smaller than the thickness of the brittle crustal layer. However, lithospheric-scale thermomechanically coupled 3-D experiments (Le Pourhiet et al., 2017) showed that such a rift linkage is also created when the horizontal distance between the rift segments is greater than the entire lithospheric thickness, even at ~ 3 –400 km. The latter observation is similar to our results, where fault segments gradually propagate toward each other and a rift linkage is created when the initial horizontal distance between the weak zones is 300 km (Figure 7). Our modeling also shows that a larger along-strike distance will increase the time required for connecting the rift segments and, therefore, more time is required for localization of deformation in the transfer zone (Figure 7).

In all modeled scenarios, the early stages of extension are characterized by a larger number of step overs with lower strike-slip fault offsets. Rift segments propagate toward the transfer zone and connect through oblique faults (Figures 3, 6, and 7). The dextral or sinistral kinematics is controlled by the spatial proximity between

structures, where closest faults connect first. This pattern changes as new faults are formed in closer spatial proximity forming new step overs. In all scenarios, more diffuse initial deformation in the transfer zone gradually evolves into one localized large step over that connects the two major rift segments. This localization and its apparent sense of shear are controlled by the gradually growing offset between the two active rift segments overlying the weak zones. Such localization occurs in our models at different times before continental breakup.

The change in step over kinematics with time is ultimately controlled by the initial strike-perpendicular distance between the weak zones (parameter d in Figure 1b and Table 1) and the variable extensional offset during the gradual opening of new subbasins. Temporal changes between sinistral and dextral apparent sense of shear along step overs in the transition zone are accentuated in our models when the initial strike-perpendicular distance is lower. In this case, a gradual opening of new rift segments is created over a smaller area and leads to a higher number of transform segments. Similarly, in the experiment where the sutures dip outward (Figure 6d) leading to opposite displacements (model Mrev), the horizontal distance between the active rift segments gradually increases with time, which creates a large dextral step over or a prototransform fault (see also Gerya, 2010b).

5. Comparison With Natural Systems

Our numerical modeling results provide a number of critical insights into the kinematics and lateral variability of extension in natural systems. Asymmetric extension and strike-slip transfer zones have been identified by high-resolution seismic and geological data in different extensional settings including back-arc systems, intracontinental rifts, and buried beneath sediments in continental passive margins. Along-strike extensional polarity changes are presently observed, for instance, in the Angola-Gabon rifted passive margin (Péron-Pinvidic et al., 2015). Extension in the Northern and Central Atlantic reactivated fossil suture zones dipping in the lithospheric mantle (Petersen & Schiffer, 2016). Such fossil sutures as weak zones are imaged by wide-angle seismic lines along these recent passive margins.

Similar asymmetric extensional structures have been recently reported from the South China Sea of SE Asia (Franke et al., 2014; Savva et al., 2014). Rifting of this basin was preceded by Mesozoic events of subduction and subsequent collision and the formation of a number of suture zones often with opposite polarities, such as the Shan, Inthanon-Bentong Raub, Nan-Sra Kaeo, or Song Ma (Metcalf, 2013). Latest Cretaceous-Eocene extension resulted in a combination between extension and strike-slip kinematics (Morley, 2002; Pubellier & Chan, 2006). A noteworthy feature of this basin is the presence of a wide strike-slip or prototransform zone in the center of the basin (Franke et al., 2014). The strike of this zone is perpendicular to the perpendicular to the above-mentioned inherited sutures, which is similar to our modeling settings. However, a detailed comparison of our model results with this area requires further studies.

The most appropriate area where a comparison with our model results can be performed is the Pannonian back-arc basin of Central Europe, where extension affected a thick lithosphere by reactivating suture zones shortly after orogenic buildup. Model results are compared with available interpreted regional seismic and well data and discussed in the context of suture zone reactivations.

5.1. Pannonian Basin System

The Pannonian Basin of Central Europe (Figure 10) is a continental back-arc basin (Horváth et al., 2015, and references therein), where the ~220–270 km of early to late Miocene extension (Balázs et al., 2017) was driven by the subduction and associated roll-back that took place in the Carpathians and/or Dinarides (Matenco et al., 2016). The Miocene extension followed pre-Neogene opening and then subsequent closure of two oceanic realms, a northern branch of the Neotethys and the Alpine Tethys (Figure 1a, Csontos & Vörös, 2004; Schmid et al., 2008). By the end of Paleogene times, successive events of shortening created a thickened orogenic area composed of two tectonic megaunits: the ALCAPA in the NW and Tisza-Dacia in the SE. Map view restorations of the region prior to the extension of the Pannonian Basin by earliest Miocene times (Figure 1a) have shown the formation of two suture zones before the onset of the main extensional events. In the south, the Neotethys suture (i.e., the north to ENE dipping Sava Suture Zone, Figure 10b) separated the Tisza-Dacia megaunit from the Dinarides (Ustaszewski et al., 2010), while in the north, the ALCAPA megaunit was thrust north to northeastward over the SW-dipping remnants of the Alpine Tethys and the

underlying Carpathian embayment (Schmid et al., 2008). This overall situation shows the existence of two inherited subduction zones with opposite polarity at the onset of extension (Figure 1a; Ustaszewski et al., 2008), which correspond and are simplified in our model setup (Figure 1b). The crust of the future Pannonian Basin contained several narrow thrust contacts over a large area (e.g., Tari et al., 1999), but in our modeling, we assumed that the major rheological contrast is localized in the mantle, attributed to fluids released during former subduction. Such a scenario is in agreement with geochemical studies from the Pannonian Basin (Kovács & Szabó, 2008).

The back-arc extension created a gradual opening of deep half-grabens located over both the ALCAPA and Tisza-Dacia megaunits from early to late Miocene (Balázs et al., 2016; Matenco et al., 2016). The contact between these units is commonly described as the Mid-Hungarian Fault/Shear Zone (MHFZ in Figure 10b). This zone is thought to have accommodated the change in polarity from the southward subduction of the Alpine Tethys in the Alps-Carpathians to the northward subduction of the Neotethys in the Dinarides in a wide transcurrent fault zone system (Csontos & Nagymarosy, 1998; Fodor et al., 1998). The main offsets along the MHFZ are interpreted as dextral during early Miocene based on the correlation and dextral offset of the Slovenian and Northern Hungarian Paleogene Basins (Sztanó & Tari, 1993). A change to sinistral kinematics has been observed for its various branches and final kinematics (Tischler et al., 2007), interpreted to be driven by the change in the stress field orientation during the Miocene (e.g., Fodor et al., 1999), controlled by the variable amount of translation and extension of the two megaunits (e.g., Fodor et al., 1998; Horváth et al., 2015; Ustaszewski et al., 2008). From the late middle Miocene times onward, extensional deformation gradually decreased in the Northern ALCAPA megaunit but continued in the southern, Tisza-Dacia megaunit, which could have resulted in an overall final sinistral kinematics along the MHFZ.

Our numerical experiments provide an additional simple dynamic model of the observed extension and associated variable kinematics along strike-slip faults in the MHFZ. These faults may represent in fact transfer zone step overs and pull-apart basins, such as the Jászág pull-apart basin (Figure 10b), that connect half-grabens situated in close proximity to, but outside the MHFZ during the extensional reactivation. This initial extensional deformation has resulted in the formation of a number of diffused dextral and sinistral offset step overs, as recorded by the observed deformation. Gradual opening of subbasins in the ALCAPA and Tisza-Dacia megaunits and the overall migration of extensional deformation lead to episodic switches between dextral and sinistral kinematics at different times along different segments of the MHFZ.

The Miocene extension migrated in space and time in the Tisza-Dacia megaunit from the Dinaridic margin of the basin toward the most extended Makó and Békés subbasins (Figure 10c) of the Pannonian Basin system until late Miocene times leaving numerous half-grabens distributed across the area (Figures 10c and 10d; see also Balázs et al., 2017). A similar deformation history and lithospheric geometry and thickness are observed when comparing a regional cross section of the Tisza-Dacia block with our modeling (Figure 10). Numerical simulation predicts a large lateral shift between the initial location of the Sava suture zone in the SW and its redistributed equivalent beneath the Moho underlying the area where extension ultimately localized in the SE part of the basin. This area is characterized by only 40-km lithospheric thickness, calculated by seismic, gravity, and thermal modeling (Tari et al., 1999). Similarly, seismic imaging has shown an anomalous thin lithospheric mantle structure (Posgay et al., 2006). We infer that this thin lithospheric area can be genetically connected to the reactivated and redistributed Sava Suture zone of the Dinarides as a weak zone beneath the base of the crust (Ustaszewski et al., 2010). Confirmation of this assumption has to come from further seismic imaging in the region. Similar to our modeling, the extensional footwall (extensional lower plate) is characterized by large offset, low-angle normal faults, and detachments that created significant footwall exhumation, while much less deformation is observed along the western Apuseni Mountains margin of the Pannonian Basin. All these observations point toward a more dynamic model of evolution of the MHFZ contact zone between the Tisza-Dacia and ALCAPA continental units that changed kinematics with time and were associated with an interaction between extensional structures located in these two units.

6. Conclusions

We conducted 3-D thermomechanical numerical experiments to investigate the extension of a thick crust and lithosphere containing suture zones with opposite subduction polarities inherited from a predating orogenic evolution. Such scenarios are inferred to have existed in nature, such as during the Pannonian Basin

extension. We modeled suture zones in the lithosphere as rheologically weak inclined layers. When such sutures have opposite polarities, their extensional reactivation creates two lithospheric-scale long-living detachment faults with opposing extensional polarities. These faults sustain large amounts of extension until the onset of oceanic spreading and migrate toward each other. As a result, asymmetric basins are formed, where deformation and associated subsidence are controlled by large-scale crustal detachments or low-angle rotated normal faults and kilometer-scale uplift of their footwalls.

Basin evolution is characterized by gradual opening of new half-grabens above the weak zones that migrate laterally and are displaced at the base of the crust by creating an effective decoupling layer. Earlier formed half-grabens become inactive and are redistributed laterally over a wide area. Modeling infers that the initial dip directions of such inherited suture zones define the subsequent extensional polarity and the associated extensional transport directions above the redistributed suture zones. The results demonstrate an active interaction along the strike of the system between the two opposite dipping weak zones, where fault segments mechanically interact and fault offsets propagate from one zone toward the other. The extensional polarity change leads to strain partitioning and the creation of wide transfer zones with sinistral and dextral step over structures.

Model results infer a change in step over kinematics between sinistral and dextral senses of apparent shear during extension, controlled by differences in extensional transport directions. Final localized deformation in the transfer zone creates one larger step over, or prototransform fault, which connects the active rift segments. The dextral or sinistral sense of shear in the transfer zone is controlled by the spatial proximity between these rift segments. Gradual opening of new subbasins during extension creates new step overs and strike-slip fault offsets that overprint previous structures in the transfer zone. This process results in kinematic switches between apparent dextral and sinistral offsets between the various subbasins.

Modeled crustal and lithospheric mantle thinning factors infer effective localization of asymmetric deformation above the weak zones. While in the area where no weak zone is present, thinning values are significantly lower and the overall deformation is more symmetrical and distributed. The initial large lateral offset between the maximum crustal and lithospheric mantle thinning factors gradually decreases during extension, although shearing of the crust and lithosphere during continental rifting is asymmetric. Symmetry of the system during extension is controlled by the location of an ESP as long as the suture represents a major rheological contrast in the lithospheric mantle. This point records maximum shearing and separates the redistributed weak zone beneath the crust and its remnant still dipping in the mantle.

Our numerical experiments provide new insights for the understanding of the extension in the Pannonian Basin and mechanics of the Mid-Hungarian Fault Zone. Extensional reactivation of the oppositely dipping Neotethys and Alpine Tethys suture zones lead to different spatial and temporal extensional kinematics in the ALCAPA and Tisza-Dacia megaunits. ESPs can be defined in the Danube Basin in the north and in the Békés Basin in the south, where asymmetric extensional deformation ultimately localized. Their boundary, the Mid-Hungarian Fault Zone, recorded switches between dextral and sinistral strike-slip and step over structures in a transfer zone during the Miocene extension and gradual opening of half-grabens in the two megaunits.

Acknowledgments

All experiments were run on the Euler cluster at ETH Zurich. 3-D visualization has been performed by ParaView. Ernst Willingshofer and Dimitrios Sokoutis are thanked for stimulating discussions. We warmly thank the two anonymous reviewers and the Editor for their thorough revision and useful suggestions of improvement. K.V. thanks funding from the German Federal Ministry for Economic Affairs and Energy (Play Type project). We note that there are no data sharing issues since all of the numerical information is provided in the figures created by solving the equations presented in the paper. Additional data can be accessed in the supporting information file.

References

- Allken, V., Huisman, R. S., & Thieulot, C. (2012). Factors controlling the mode of rift interaction in brittle-ductile coupled systems: A 3D numerical study. *Geochemistry, Geophysics, Geosystems*, 13, Q05010. <https://doi.org/10.1029/2012GC004077>
- Antobreh, A. A., Faleide, J. I., Tsikalas, F., & Planke, S. (2009). Rift-shear architecture and tectonic development of the Ghana margin deduced from multichannel seismic reflection and potential field data. *Marine and Petroleum Geology*, 26, 345–368.
- Balázs, A., Burov, E., Matenco, L., Vogt, K., Francois, T., & Cloetingh, S. (2017). Symmetry during the syn- and post-rift evolution of extensional back-arc basins: The role of inherited orogenic structures, Earth planet. *Science Letters*, 462, 86–98.
- Balázs, A., Matenco, L., Magyar, I., Horváth, F., & Cloetingh, S. (2016). The link between tectonics and sedimentation in back-arc basins: New genetic constraints from the analysis of the Pannonian Basin. *Tectonics*, 35, 1526–1559. <https://doi.org/10.1002/2015TC004109>
- Beaumont, C., Muñoz, J. A., Hamilton, J., & Fullsack, P. (2000). Factors controlling the Alpine evolution of Central Pyrenees inferred from the comparison of observations and geodynamical models. *Journal of Geophysical Research*, 105(B4), 8121–8145. <https://doi.org/10.1029/1999JB900390>
- Bellahsen, N., Fournier, M., d'Acremont, E., Leroy, S., & Daniel, J. (2006). Fault reactivation and rift localization: Northeastern Gulf of Aden margin. *Tectonics*, 25, TC1007. <https://doi.org/10.1029/2004TC001626>
- Brun, J.-P. (1999). Narrow rifts versus wide rifts: Inferences for the mechanics of rifting from laboratory experiments. *Philosophical Transactions of the Royal Society of London*, 357, 695–710.

- Brune, S., Corti, G., & Ranalli, G. (2017). Controls of inherited lithospheric heterogeneity on rift linkage: Numerical and analog models of interaction between the Kenyan and Ethiopian rifts across the Turkana depression. *Tectonics*, *36*, 1767–1786. <https://doi.org/10.1002/2017TC004739>
- Buck, W. R. (1988). Flexural rotation of normal faults. *Tectonics*, *5*, 959–973. <https://doi.org/10.1029/TC0071005p00959>
- Buiter, S., & Torsvik, T. H. (2014). A review of Wilson cycle plate margins: A role for mantle plumes in continental break-up along sutures? *Gondwana Research*, *26*(2), 627–653. <https://doi.org/10.1016/j.gr.2014.02.007>
- Burov, E., & Poliakov, A. (2001). Erosion and rheology controls on syn and post-rift evolution: Verifying old and new ideas using a fully coupled numerical model. *Journal of Geophysical Research*, *106*(B8), 16,461–16,481. <https://doi.org/10.1029/2001JB000433>
- Chorowicz, J. (1989). Transfer and transform fault zones in continental rifts: Examples in the Afro-Arabian Rift system. *Journal of African Earth Sciences*, *8*, 203–214.
- Cloetingh, S., Burov, E., Matenco, L., Beekman, F., Roure, F., & Ziegler, P. A. (2013). The Moho in extensional tectonic settings: Insights from thermo-mechanical models. *Tectonophysics*, *609*, 558–604. <https://doi.org/10.1016/j.tecto.2013.06.010>
- Corti, G. (2008). Control of rift obliquity on the evolution and segmentation of the main Ethiopian rift. *Nature Geoscience*, *1*, 258–262.
- Corti, G. (2009). Continental rift evolution: From rift initiation to incipient break-up in the Main Ethiopian Rift, East Africa. *Earth-Science Reviews*, *96*(1–2), 1–53. <https://doi.org/10.1016/j.earscirev.2009.06.005>
- Cramer, F., Schmeling, H., Golabek, G. J., Duretz, T., Orendt, R., Buiter, S. J. H., et al. (2012). A comparison of numerical surface topography calculations in geodynamic modelling: An evaluation of the ‘sticky air’ method. *Geophysical Journal International*, *189*(1), 38–54. <https://doi.org/10.1111/j.1365-246X.2012.05388.x>
- Crosby, A. G., White, N. J., Edwards, G. R. H., Thompson, M., Corfield, R., & Mackay, L. (2011). Evolution of deep-water rifted margins: Testing depth-dependent extensional models. *Tectonics*, *30*, TC1004. <https://doi.org/10.1029/2010TC002687>
- Csontos, L., & Nagymarosy, A. (1998). The Mid-Hungarian line: A zone of repeated tectonic inversions. *Tectonophysics*, *29*, 51–71.
- Csontos, L., & Vörös, A. (2004). Mesozoic plate tectonic reconstruction of the Carpathian region. *Palaeogeography, Palaeoclimatology, Palaeoecology*, *210*(1), 1–56. <https://doi.org/10.1016/j.palaeo.2004.02.033>
- Dias, A. E., Lavier, L. L., & Hayman, N. W. (2015). Conjugate rifted margins width and asymmetry: The interplay between lithospheric strength and thermomechanical processes. *Journal of Geophysical Research: Solid Earth*, *120*, 8672–8700. <https://doi.org/10.1002/2015JB012074>
- Dunbar, J. A., & Sawyer, D. S. (1988). Continental rifting at pre-existing lithospheric weaknesses. *Nature*, *333*(6172), 450–452. <https://doi.org/10.1038/333450a0>
- Duretz, T., Petri, B., Mohn, G., Schmalholz, S. M., Schenker, F. L., & Muntener, O. (2016). The importance of structural softening for the evolution and architecture of passive margins. *Scientific Reports*, *6*(1), 38704. <https://doi.org/10.1038/srep38704>
- Faccenna, C., Becker, T. W., Auer, L., Billi, A., Boschi, L., Brun, J. P., et al. (2014). Mantle dynamics in the Mediterranean. *Reviews of Geophysics*, *52*(3), 283–332. <https://doi.org/10.1002/2013RG000444>
- Fodor, L., Csontos, L., Bada, G., Györfi, I., & Benkovics, L. (1999). Tertiary tectonic evolution of the Pannonian Basin system and neighbouring orogens: A new synthesis of paleostress data. In B. Durand, L. Jolivet, F. Horvath, & M. Seranne (Eds.), *The Mediterranean basins: Tertiary extension within the Alpine orogen* (pp. 295–334). London: The Geological Society.
- Fodor, L., Jelen, B., Márton, E., Skaberne, D., Čar, J., & Vrabec, M. (1998). Miocene-Pliocene tectonic evolution of the Slovenian Periadriatic fault: Implications for Alpine-Carpathian extrusion models. *Tectonics*, *17*(5), 690–709. <https://doi.org/10.1029/98TC01605>
- Franke, D., Savva, D., Pubellier, M., Steuer, S., Mouly, B., Auxietre, J., et al. (2014). The final rifting evolution in the South China Sea. *Marine and Petroleum Geology*, *58*, 704–720. <https://doi.org/10.1016/j.marpetgeo.2013.11.020>
- Gerya, T. V. (2010a). *Introduction to numerical geodynamic modelling* (p. 345). Cambridge, UK: Cambridge University Press.
- Gerya, T. V. (2010b). Dynamical instability produces transform faults at mid-ocean ridges. *Science*, *329*(5995), 1047–1050. <https://doi.org/10.1126/science.1191349>
- Gerya, T. V. (2013a). Three-dimensional thermomechanical modeling of oceanic spreading initiation and evolution. *Physics of the Earth and Planetary Interiors*, *214*, 35–52. <https://doi.org/10.1016/j.pepi.2012.10.007>
- Gerya, T. V. (2013b). Initiation of transform faults at rifted continental margins: 3D petrological-thermomechanical modeling and comparison to the Woodlark Basin. *Petrology*, *21*(6), 550–560. <https://doi.org/10.1134/S0869591113060039>
- Gerya, T. V., & Yuen, D. A. (2007). Robust characteristics method for modelling multiphase visco-elasto-plastic thermo-mechanical problems. *Physics of the Earth and Planetary Interiors*, *163*(1–4), 83–105. <https://doi.org/10.1016/j.pepi.2007.04.015>
- Heron, P. J., Pysklywec, R. N., & Stephenson, R. (2016). Lasting mantle scars lead to perennial plate tectonics. *Nature Communications*, *7*, 11834. <https://doi.org/10.1038/ncomms11834>
- Horváth, F., Musitz, B., Balázs, A., Végh, A., Uhrin, A., Nádor, A., et al. (2015). Evolution of the Pannonian Basin and its geothermal resources. *Geothermics*, *53*, 328–352. <https://doi.org/10.1016/j.geothermics.2014.07.009>
- Huet, B., Le Pourhiet, L., Labrousse, L., Burov, E. B., & Jolivet, L. (2011). Formation of metamorphic core complex in inherited wedges: A thermomechanical modelling study, Earth planet. *Science Letters*, *309*, 249–257.
- Huismans, R., & Beaumont, C. (2011). Depth-dependent extension, two-stage breakup and cratonic underplating at rifted margins. *Nature*, *473*(7345), 74–78. <https://doi.org/10.1038/nature09988>
- Jolivet, L., Faccenna, C., Huet, B., Labrousse, L., Le Pourhiet, L., Lacombe, O., et al. (2013). Aegean tectonics: Strain localisation, slab tearing and trench retreat. *Tectonophysics*, *597*, 1–33.
- Katayama, I., & Karato, S. (2008). Low-temperature, high-stress deformation of olivine under water-saturated conditions. *Physics of the Earth and Planetary Interiors*, *168*(3–4), 125–133. <https://doi.org/10.1016/j.pepi.2008.05.019>
- Katz, R. F., Spiegelman, M., & Langmuir, C. H. (2003). A new parameterization of hydrous mantle melting. *Geochemistry, Geophysics, Geosystems*, *4*(9), 1073. <https://doi.org/10.1029/2002GC000433>
- Keranen, K., & Klempner, S. L. (2008). Discontinuous and diachronous evolution of the Main Ethiopian Rift: Implications for development of continental rifts, Earth planet. *Science Letters*, *265*, 96–111.
- Kovács, I., & Szabó, C. (2008). Middle Miocene volcanism in the vicinity of the middle Hungarian zone: Evidence for an inherited enriched mantle source. *Journal of Geodynamics*, *45*(1), 1–17. <https://doi.org/10.1016/j.jog.2007.06.002>
- Lavier, L., & Manatschal, G. (2006). A mechanism to thin the continental lithosphere at magma-poor margins. *Nature*, *440*(7082), 324–328. <https://doi.org/10.1038/nature04608>
- Le Pourhiet, L., Burov, E., & Moretti, I. (2004). Rifting through a stack of inhomogeneous thrusts (the dipping pie concept). *Tectonics*, *23*, TC4005. <https://doi.org/10.1029/2003TC001584>
- Le Pourhiet, L., May, D. A., Huille, L., Watremez, L., & Leroy, S. (2017). A genetic link between transform and hyper-extended margins, Earth planet. *Science Letters*, *465*, 184–192.
- Liao, J., & Gerya, T. (2014). Influence of lithospheric mantle stratification on craton extension: Insight from two-dimensional thermo-mechanical modeling. *Tectonophysics*, *631*, 50–64. <https://doi.org/10.1016/j.tecto.2014.01.020>

- Liao, J., & Gerya, T. (2015). From continental rifting to seafloor spreading: Insight from 3D thermo-mechanical modeling. *Gondwana Research*, 28(4), 1329–1343. <https://doi.org/10.1016/j.gr.2014.11.004>
- Lister, G. S., Etheridge, M. A., & Symonds, P. A. (1986). Detachment faulting and the evolution of passive continental margins. *Geology*, 14(3), 246–250. [https://doi.org/10.1130/0091-7613\(1986\)14<246:DFATEO>2.0.CO;2](https://doi.org/10.1130/0091-7613(1986)14<246:DFATEO>2.0.CO;2)
- Luth, S., Willingshofer, E., Sokoutis, D., & Cloetingh, S. (2010). Analogue modelling of continental collision: Influence of plate coupling on mantle lithosphere subduction, crustal deformation and surface topography. *Tectonophysics*, 484(1-4), 87–102. <https://doi.org/10.1016/j.tecto.2009.08.043>
- Manatschal, G. (2004). New models for evolution of magma-poor rifted margins based on a review of data and concepts from West Iberia and Alps. *International Journal of Earth Sciences*, 93(3), 432–466. <https://doi.org/10.1007/s00531-004-0394-7>
- Manatschal, G., Lavier, L., & Chenin, P. (2015). The role of inheritance in structuring hyperextended rift systems: Some considerations based on observations and numerical modeling. *Gondwana Research*, 27(1), 140–164. <https://doi.org/10.1016/j.gr.2014.08.006>
- Matenco, L., Munteanu, I., ter Borgh, M., Stanica, A., Tilita, M., Lericolais, G., et al. (2016). The interplay between tectonics, sediment dynamics and gateways evolution in the Danube system from the Pannonian Basin to the western Black Sea. *Science of the Total Environment*, 543(Pt A), 807–827. <https://doi.org/10.1016/j.scitotenv.2015.10.081>
- Metcalfe, I. (2002). Permian tectonic framework and palaeogeography of SE Asia. *Journal of Asian Earth Sciences*, 20(6), 551–566. [https://doi.org/10.1016/S1367-9120\(02\)00022-6](https://doi.org/10.1016/S1367-9120(02)00022-6)
- Metcalfe, I. (2013). Gondwana dispersion and Asian accretion: Tectonic and palaeogeographic evolution of eastern Tethys. *Journal of Asian Earth Sciences*, 66, 1–33. <https://doi.org/10.1016/j.jseaeas.2012.12.020>
- Michon, L., & Sokoutis, D. (2005). Interaction between structural inheritance and extension direction during graben and depocentre formation: An experimental approach. *Tectonophysics*, 409(1-4), 125–146. <https://doi.org/10.1016/j.tecto.2005.08.020>
- Molli, G., & Malavieille, J. (2011). Orogenic processes and the Corsica/Apeninnes geodynamic evolution: Insights from Taiwan. *International Journal of Earth Sciences*, 100(5), 1207–1224. <https://doi.org/10.1007/s00531-010-0598-y>
- Morley, C. K. (2002). A tectonic model for the Tertiary evolution of strike-slip faults and rift basins in SE Asia. *Tectonophysics*, 347(4), 189–215. [https://doi.org/10.1016/S0040-1951\(02\)00061-6](https://doi.org/10.1016/S0040-1951(02)00061-6)
- Morley, C. K., Nelson, R. A., Patton, T. L., & Munn, S. G. (1990). Transfer zones in the East African Rift System and their relevance to hydrocarbon exploration in rifts. *AAPG Bulletin*, 74, 1234–1253.
- Munteanu, I., Willingshofer, E., Matenco, L., Sokoutis, D., & Cloetingh, S. (2014). Far-field contractional polarity changes in models and nature, Earth planet. *Science Letters*, 395, 101–115.
- Naliboff, J. B., Buiter, S. J. H., Péron-Pinvidic, G., Osmundsen, P. T., & Tetreault, Y. (2017). Complex fault interaction controls continental rifting. *Nature Communications*, 8(1), 1179. <https://doi.org/10.1038/s41467-017-00904-x>
- Péron-Pinvidic, G., Manatschal, G., Masini, E., Sutra, E., Flament, J. M., Hauptert, I., & Unternehr, P. (2015). Unravelling the along-strike variability of the Angola-Gabon rifted margin: A mapping approach. *Geological Society of London, Special Publication*, 438(1), 49–76. <https://doi.org/10.1144/SP438.1>
- Petersen, K., & Schiffer, C. (2016). Wilson cycle passive margins: Control of orogenic inheritance on continental breakup. *Gondwana Research*, 39, 131–144. <https://doi.org/10.1016/j.gr.2016.06.012>
- Posgay, K., Bodoky, T., Hajnal, Z., Toth, T. M., Fancsik, T., Hegedus, E., et al. (2006). Interpretation of subhorizontal crustal reflections by metamorphic and rheologic effects in the eastern part of the Pannonian Basin. *Geophysical Journal International*, 167(1), 187–203. <https://doi.org/10.1111/j.1365-246X.2006.03000.x>
- Pubellier, M., & Chan, L. S. (2006). *Structural map of Cenozoic structures of South China and North Vietnam Coastal*. Hong Kong: CGMW.
- Püthe, C., & Gerya, T. V. (2013). Dependence of mid-ocean ridge morphology on spreading rate in numerical 3-D models. *Gondwana Research*, 25, 270–283.
- Ranalli, G. (1995). *Rheology of the Earth* (p. 334). London, UK: Springer.
- Rosenbaum, G., Regenauer-Lieb, K., & Weinberg, R. (2005). Continental extension: From core complexes to rigid block faulting. *Geology*, 33(7), 609–612. <https://doi.org/10.1130/G21477.1>
- Savva, D., Pubellier, M., Franke, D., Chamot-Rooke, N., Meresse, F., Steuer, S., & Auxietre, J. L. (2014). Different expressions of rifting on the South China Sea margins. *Marine and Petroleum Geology*, 58, 579–598. <https://doi.org/10.1016/j.marpetgeo.2014.05.023>
- Schmid, S., Bernoulli, D., Fügenschuh, B., Matenco, L., Schefer, S., Schuster, R., et al. (2008). The Alpine-Carpathian-Dinaridic orogenic system: Correlation and evolution of tectonic units. *Swiss Journal of Geosciences*, 101(1), 139–183. <https://doi.org/10.1007/s00015-008-1247-3>
- Searle, R. C., Thomas, M. V., & Jones, E. J. W. (1994). Morphology and tectonics of the Romanche transform and its environs. *Marine Geophysical Researches*, 16(6), 427–453. <https://doi.org/10.1007/BF01270518>
- Sztanó, O., & Tari, G. (1993). Early Miocene basin evolution in Northern Hungary: Tectonics and Eustasy. *Tectonophysics*, 226(1-4), 485–502. [https://doi.org/10.1016/0040-1951\(93\)90134-6](https://doi.org/10.1016/0040-1951(93)90134-6)
- Tari, G., Dovenyi, P., Dunkl, I., Horvath, F., Lenkey, L., Ștefănescu, M., et al. (1999). Lithospheric structure of the Pannonian Basin derived from seismic, gravity and geothermal data. In B. Durand, et al. (Eds.), *The Mediterranean basins: Extension within the Alpine orogen*, *Geol. Soc. Spec. Publ.* (Vol. 156, pp. 215–250).
- Tesaro, M., Kaban, M. K., & Cloetingh, S. (2009). A new thermal and rheological model of the European lithosphere. *Tectonophysics*, 476(3-4), 478–495. <https://doi.org/10.1016/j.tecto.2009.07.022>
- Tischler, M., Gröger, H., Fügenschuh, B., & Schmid, S. M. (2007). Miocene tectonics of the Maramures area (Northern Romania): Implications for the Mid-Hungarian Fault Zone. *International Journal of Earth Sciences*, 96(3), 473–496. <https://doi.org/10.1007/s00531-006-0110-x>
- Turcotte, D. L., & Schubert, G. (2002). *Geodynamics*. Cambridge, UK: Cambridge University Press. <https://doi.org/10.1017/CBO9780511807442>
- Ustaszewski, K., Kounov, A., Schmid, S. M., Schaltegger, U., Krenn, E., Frank, W., & Fügenschuh, B. (2010). Evolution of the Adria-Europe plate boundary in the northern Dinarides: From continent-continent collision to back-arc extension. *Tectonics*, 29, TC6017. <https://doi.org/10.1029/2010tc002668>
- Ustaszewski, K., Schmid, S., Fügenschuh, B., Tischler, M., Kissling, E., & Spakman, W. (2008). A map-view restoration of the Alpine-Carpathian-Dinaridic system for the early Miocene. *Swiss Journal of Geosciences*, 101, 273–294.
- Wernicke, B. (1985). Uniform-sense normal simple shear of the continental lithosphere. *Canadian Journal of Earth Sciences*, 22(1), 108–125. <https://doi.org/10.1139/e85-009>
- Willett, S. D., & Brandon, M. T. (2002). On steady state in mountain belts. *Geology*, 30(2), 175–178. [https://doi.org/10.1130/0091-7613\(2002\)030<0175:OSSIMB>2.0.CO;2](https://doi.org/10.1130/0091-7613(2002)030<0175:OSSIMB>2.0.CO;2)
- Zwaan, F., Schreurs, G., Naliboff, J., & Buiter, S. H. (2016). Insights into the effects of oblique extension on continental rift interaction from 3D analogue and numerical models. *Tectonophysics*, 693, 239–260. <https://doi.org/10.1016/j.tecto.2016.02.036>